Article

Current Biology

Opto-katanin, an optogenetic tool for localized, microtubule disassembly

Graphical abstract

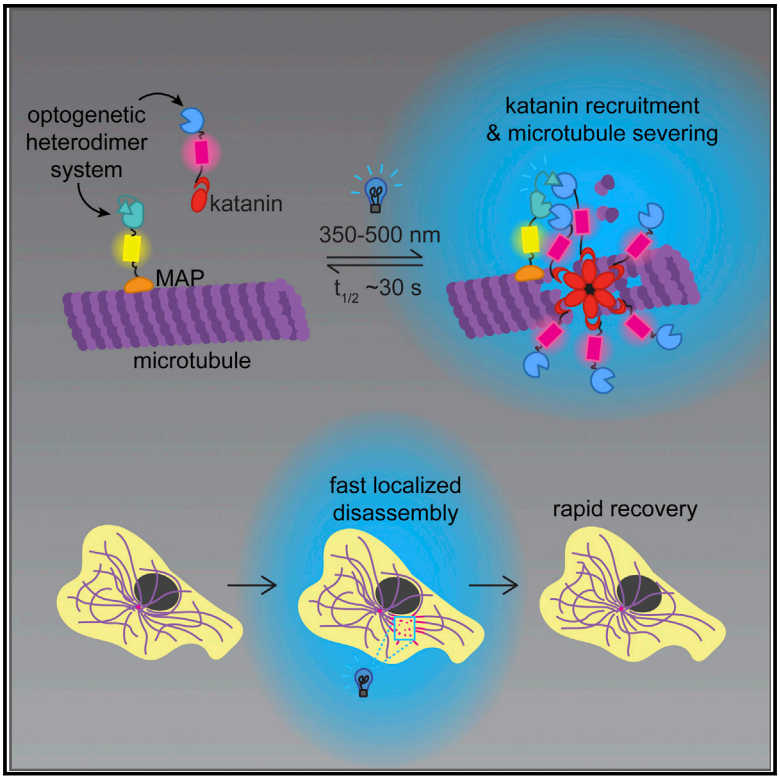

Highlights

- Blue-light-induced katanin targeting triggers fast, localized microtubule clearance
- Opto-katanin-mediated microtubule disassembly is rapidly reversible
- Different microtubule anchors can be used for katanin targeting and severing
- Opto-katanin can be employed to locally block transport and probe cell mechanics

Authors

Joyce C.M. Meiring, Ilya Grigoriev, Wilco Nijenhuis, Lukas C. Kapitein, Anna Akhmanova

Correspondence

a.akhmanova@uu.nl

In brief

Meiring et al. engineer an optogenetic tool for fast, reversible, and highly localized disassembly of microtubules and maintenance of microtubule-free areas in cells by controlling the recruitment of katanin. This tool was used to study microtubule-dependent ER and cargo dynamics and to show that microtubule bundles can exert forces on the nucleus.

Meiring et al., 2022, Current Biology *32*, 4660–4674
November 7, 2022
https://doi.org/10.1016/j.cub.2022.09.010

CellPress

CellPress
OPEN ACCESS

Current Biology

Article

Opto-katanin, an optogenetic tool for localized, microtubule disassembly

Joyce C.M. Meiring,[1,3] Ilya Grigoriev,[1] Wilco Nijenhuis,[1,2] Lukas C. Kapitein,[1,2] and Anna Akhmanova[1,4,*]
[1]Cell Biology, Neurobiology and Biophysics, Department of Biology, Faculty of Science, Utrecht University, Padualaan, Utrecht 3584 CS, the Netherlands
[2]Center for Living Technologies, Eindhoven-Wageningen-Utrecht Alliance, UMC Utrecht, Utrecht 3584 CB, the Netherlands
[3]Twitter: @psychescope
[4]Lead contact
*Correspondence: a.akhmanova@uu.nl
https://doi.org/10.1016/j.cub.2022.09.010

SUMMARY

Microtubules are cytoskeletal polymers that separate chromosomes during mitosis and serve as rails for intracellular transport and organelle positioning. Manipulation of microtubules is widely used in cell and developmental biology, but tools for precise subcellular spatiotemporal control of microtubules are currently lacking. Here, we describe a light-activated system for localized recruitment of the microtubule-severing enzyme katanin. This system, named opto-katanin, uses targeted illumination with blue light to induce rapid, localized, and reversible microtubule depolymerization. This tool allows precise clearing of a subcellular region of microtubules while preserving the rest of the microtubule network, demonstrating that regulation of katanin recruitment to microtubules is sufficient to control its severing activity. The tool is not toxic in the absence of blue light and can be used to disassemble both dynamic and stable microtubules in primary neurons as well as in dividing cells. We show that opto-katanin can be used to locally block vesicle transport and to clarify the dependence of organelle morphology and dynamics on microtubules. Specifically, our data indicate that microtubules are not required for the maintenance of the Golgi stacks or the tubules of the endoplasmic reticulum but are needed for the formation of new membrane tubules. Finally, we demonstrate that this tool can be applied to study the contribution of microtubules to cell mechanics by showing that microtubule bundles can exert forces constricting the nucleus.

INTRODUCTION

Microtubules have been implicated in nearly every step of cell physiology. They separate chromosomes during cell division, serve as tracks for long-range intracellular transport and organelle positioning, control cell and organelle morphology, and regulate adhesion turnover in migrating cells.[1–3] Given the broad significance of microtubules, tools for their discrete manipulation are highly sought after to study the role of microtubules in specific processes while minimizing global cell perturbation. Laser ablation has been used to perform localized microtubule cutting within cells;[4,5] it is an effective tool for targeted ablation of diverse cellular structures, notably the destruction of centrosomes.[5] However, this technique does not discriminate between microtubules and other cellular components. It can therefore cause undesired side effects and cannot be applied to large cell regions. Optogenetic approaches have been very successful in exerting both specific and targeted subcellular effects, for example, steering of migrating cells by reducing the rate and persistence of microtubule growth using a photo-inactivated end-binding protein 1 (EB1).[6]

Here, we set out to achieve potent, localized, microtubule-specific disassembly by developing an optogenetic tool for microtubule severing. For this, we made use of the improved light-induced dimerizer (iLID) system, consisting of an optimized light-oxygen-voltage-sensing domain 2 (LOV2) domain derived from *Avena sativa* conjugated with the bacterially derived SspB-binding peptide SsrA.[7] SsrA is sterically blocked when LOV2 is in the dark state but becomes uncaged upon blue light activation of LOV2 and available to bind SspB. The iLID-SspB system offers a larger dynamic range than older systems and a more than 50-fold increase in affinity upon activation, and its components do not oligomerize, thus avoiding aggregate-induced perturbations of cell functions.[7]

Previously, an optogenetic microtubule-disrupting tool was developed in the form of a light recruitable microtubule catastrophe promoter, kinesin-13.[8] However, inducible recruitment of kinesin-13 was not sufficient to locally deplete all microtubules, likely because kinesin-13 triggers the disassembly of growing microtubule ends but is less efficient in depolymerizing stable microtubule lattices.[9] Since we wanted to develop a tool that could disassemble both dynamic and stable microtubules, we opted to use a microtubule-severing enzyme instead. We combined the iLID-SspB system with the microtubule-severing enzyme katanin. Katanin consists of p60 and p80 subunits, where p60 is the enzymatically active subunit that forms a hexamer that interacts with β-tubulin tails to extrude tubulin dimers from the microtubule lattice.[10–13] Previous reports showed that

CellPress
OPEN ACCESS

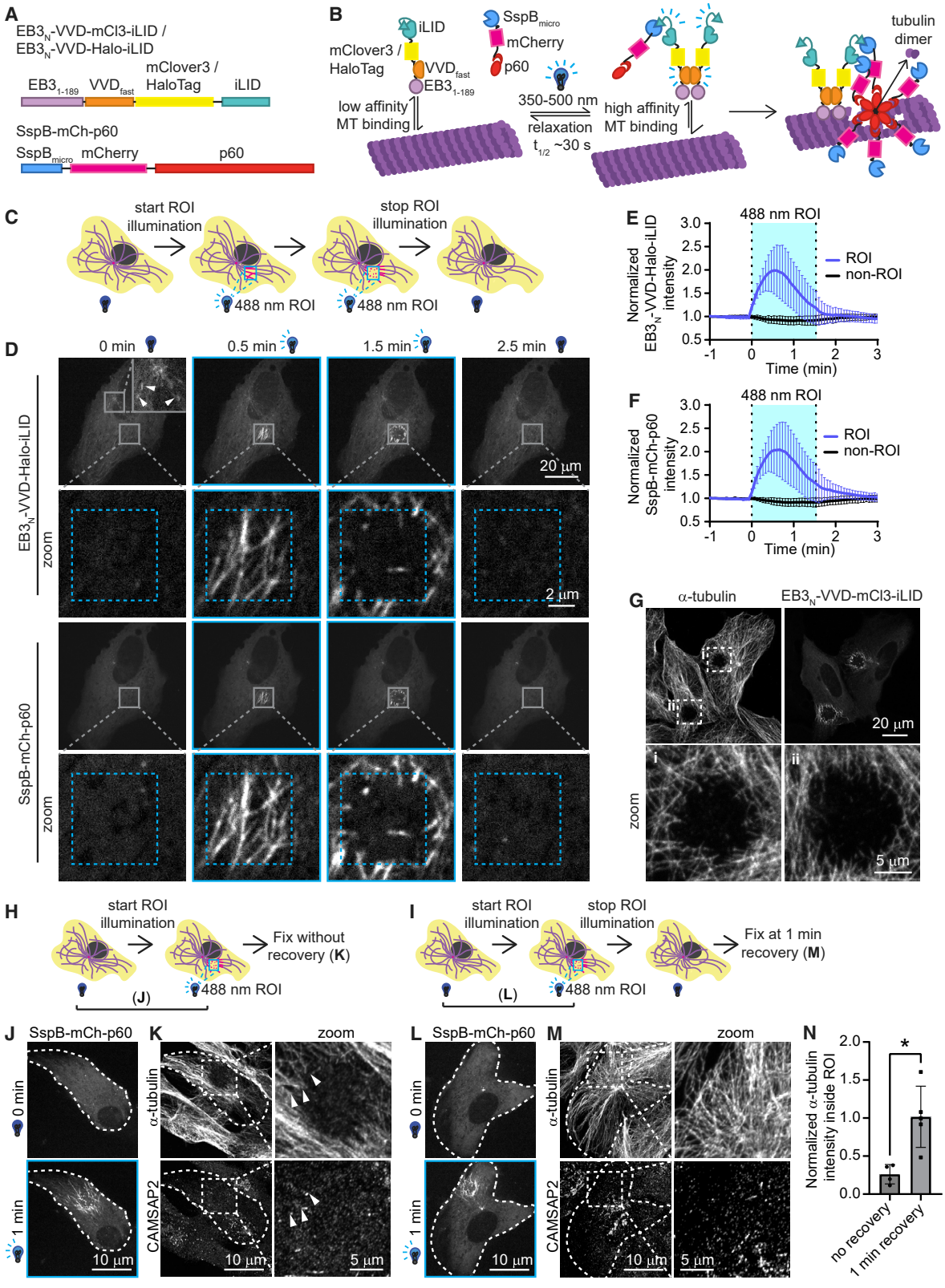

(legend on next page)

mammalian p60 has low microtubule-binding affinity on its own and requires co-factors like katanin p80, calmodulin-regulated spectrin-associated protein 3 (CAMSAP3), and abnormal spindle-like microcephaly-associated protein (ASPM) for its recruitment to microtubules and microtubule-severing activity.[14–16] Since p60-severing activity depends on its recruitment to microtubules, we considered this enzyme to be a promising candidate for an optogenetic tool. We tested an assortment of microtubule-binding proteins and domains to arrive at an optimal microtubule-binding anchor, an EB3 microtubule-binding domain with a VVD_{fast}-based reversible blue light-sensitive homodimerization domain.[17] In utilizing two separate blue light-sensitive systems, VVD_{fast} to control recruitment of the anchor to microtubules and iLID-SspB to control the recruitment of katanin to microtubules, we were able to minimize dark-state activity and off-target binding to limit the impact on normal microtubule architecture. Our system, which we named "opto-katanin," could induce highly localized and rapidly reversible removal of microtubules in a cell region within 1.5 min in cultured cancer cells and 10 min in neurons. We demonstrate that opto-katanin-mediated microtubule severing could be combined with imaging of organelles to observe the impact of local microtubule disassembly on transport and organelle morphology. Lastly, we show how opto-katanin may be implemented in a stable cell line and used to halt cell progression through mitosis.

RESULTS

Localized and reversible microtubule disassembly by light-controlled katanin recruitment

In order to make a system that could recruit katanin to microtubules in a light-dependent manner, we designed a microtubule anchor incorporating iLID and a p60 construct linked to $SspB_{micro}$. The microtubule-binding domain of EB3 ($EB3_N$) was used as a microtubule anchor. Artificial EB dimer constructs have been reported to bind the microtubule lattice with higher affinity than artificial EB monomers.[18,19] Therefore we incorporated an optimized blue light-sensitive optogenetic homodimerization domain with fast reversibility known as VVD_{fast}.[17] With a two-step activation consisting of dimerization of VVD and unfolding of iLID, we hoped to reduce dark-state activity. This also aimed to reduce competition of the anchor construct with endogenously expressed microtubule-associated proteins (MAPs). The $EB3_N$ microtubule anchor and p60 construct were labeled with mClover3 (mCl3) or HaloTag (Halo) with a far red HaloTag dye and mCherry (mCh), respectively, so that their expression levels and localization could be assessed without activating iLID-SspB and VVD_{fast} (Figure 1A). Flexible GGGGS linkers were inserted between protein domains to support proper protein folding and function (Figure 1A). We expected that blue light would trigger homodimerization of $EB3_N$-VVD-mCl3-iLID or $EB3_N$-VVD-Halo-iLID, which would enhance microtubule binding affinity, and simultaneously unfold iLID, allowing binding of SspB-mCh-p60, recruiting it to microtubules and thus prompting its disassembly (Figure 1B).

We tested local disassembly and reversibility by first imaging without blue light illumination to set a baseline, then pulsing cells with blue light in a region of interest (ROI) to activate optogenetic constructs, followed by another period without blue light illumination to observe the time required for constructs to return to their dark-state localization (Figure 1C). Prior to blue light illumination, $EB3_N$-VVD-Halo-iLID was slightly enriched at microtubule plus ends, in agreement with the data showing that the monomeric microtubule-binding domain of EB3 can weakly bind to growing microtubule plus ends[19] (white arrows, Figure 1D; Video S1). SspB-mCh-p60 was observed to be enriched at the centrosome but was mostly cytoplasmic, consistent with prior localization studies of p60 (Figure 1D; Video S1).[10,15] Upon localized blue light pulsing, both $EB3_N$-VVD-Halo-iLID and SspB-mCh-p60 were recruited to microtubules inside the

Figure 1. Converting katanin into an optogenetic tool for localized and reversible microtubule disassembly

(A) Overview of opto-katanin constructs; protein domains are separated by flexible GGGGS linkers.

(B) A scheme showing the mechanism of microtubule disassembly by opto-katanin. In the dark state, $EB3_N$-VVD-mCl3-iLID or $EB3_N$-VVD-Halo-iLID constructs bind microtubules with low affinity, and iLID does not bind SspB. Upon blue light activation, VVD_{fast} homodimerizes enabling high-affinity microtubule binding of EB3 microtubule-binding domain. Blue light also causes iLID to change conformation, revealing a SsrA domain that engages with SspB, thus recruiting SspB-mCh-p60 to microtubules and promoting microtubule disassembly by p60.

(C) Scheme of experimental setup: cells co-transfected with opto-katanin constructs are locally pulsed with blue light to induce localized construct recruitment and microtubule disassembly. Blue light pulsing is then stopped to observe the off rate of optogenetic constructs and local microtubule recovery.

(D–F) U2OS cells co-transfected with SspB-mCh-p60 and $EB3_N$-VVD-Halo-iLID imaged on a spinning disc microscope. Cells are imaged for 0.5 min before locally pulsing with blue light inside ROI (marked by blue dashed box) for 1.5 min and subsequently imaged without blue light pulsing, see also Video S1. In (D), representative stills are shown at the indicated time points before (0 min), during (0.5 and 1.5 min), and after (2.5 min) local blue light illumination. Inset shows $EB3_N$-VVD-Halo-iLID at microtubule plus ends, highlighted by white arrows. (E) and (F) show quantification of fluorescence intensity of $EB3_N$-VVD-Halo-iLID (E) and SspB-mCh-p60 (F) inside blue light pulsed areas (ROI) and comparable sites not pulsed with blue light (non-ROI) in the same cell for the indicated channels normalized to the average of the first 5 time points. n = 17 cells across 3 independent experiments, graphs show mean ± SD.

(G) U2OS cells co-transfected with SspB-mCh-p60 and $EB3_N$-VVD-mCl3-iLID, locally illuminated with blue light to induce microtubule severing, fixed without recovery from blue light illumination, stained for α-tubulin and imaged on an Airyscan confocal microscope; maximum intensity projections are shown. Zoom shows two areas where microtubules were locally severed using opto-katanin.

(H and I) Scheme of experimental setup: cells co-transfected with opto-katanin constructs are locally pulsed with blue light to induce localized microtubule severing. Cells are either fixed directly after microtubule severing (H) or blue light pulsing is switched off and cells are fixed after 1 min recovery (I).

(J–N) RPE1 cells co-transfected with $EB3_N$-VVD-Halo-iLID and SspB-mCh-p60 locally pulsed with blue light on a spinning disc confocal microscope. Cells were either fixed immediately (J and K) or after 1 min without local blue light pulsing (L and M). In (J) and (L), cell before (0 min) and during local microtubule severing (1 min) is shown. (K) and (M) show fixed cells immunostained for α-tubulin and CAMSAP2 and imaged on an Airyscan confocal microscope; maximum intensity projections are shown. Occasionally severed microtubule ends have short CAMSAP2 labeling as highlighted by white arrows (K), and α-tubulin staining intensity was quantified inside the area in which microtubules were severed and normalized to whole-cell intensity (N). n = 4–5 cells per treatment group across 3 independent experiments, graph shows mean ± SD with individual cell measurements shown as dot points. *$p < 0.05$.

See also Figure S1 and Videos S1 and S2.

Table 1. Performance of anchor constructs in microtubule binding, bundling, and severing

Anchor construct	MT binding	MT bundling	MT severing
$EB3_N$ (1-189)-VVD_{fast}-mCl3-iLID *	+ dark/++ lit	–	++
$EB3_N$ (1-189)-VVD_{fast}-Halo-iLID *	+ dark/++ lit	–	++
iLID-mCl3-DCX *	++	–	++
iLID-mCl3-MAP7	++	++	±
iLID-mCl3-$MAP7_N$(1-301) *	++	–	++
iLID-mCl3-$MAP7_{MTBD}$(59-170)	++	–	++
iLID-mCl3-MAP7D3 *	++	–	++
iLID-mCl3-$MAP7D3_N$(1-309)	+	–	++
iLID-mCl3-$MAP7D3_{MTBD}$(55-174)	+	–	++
$CLIP115_N$(1-309)-mCl3-iLID *	+	–	++
iLID-mCl3-Tau0N4R	++	++	±
iLID-mCl3-miniTau0N4R(140-342)	++	+	++
iLID-mCl3-Tau0N4R $_{MTBD}$(186-310)	–	–	–
iLID-mCl3-Tau0N3R	++	++	±
iLID-mCl3-MAP2C	++	++	–
iLID-mCl3-$MAP2C_{MTBD}$(300-393)	–	–	–

Severing performance was assessed in the context of co-transfection with SspB-mCh-p60 and live-cell imaging with blue light illumination. ++ high, + moderate, ± poor, – not observed. Constructs with an * are shown in Figure 2.
See Figure S2 for details on grading metrics.

ROI, reaching peak enrichment approximately 30 s after commencing blue light pulsing, before intensity dropped due to microtubule severing (Figures 1D–1F; Video S1). After microtubules were disassembled inside the ROI, $EB3_N$-VVD-Halo-iLID and SspB-mCh-p60 became enriched on microtubules bordering the ROI due to diffusion of activated constructs in the absence of microtubules to bind (Figure 1D). If blue light illumination was continued, microtubules bordering the ROI were also disassembled, and to prevent this, illumination was stopped after 1.5 min, just after microtubules inside the ROI were disassembled. Constructs redispersed in under 1 min of stopping blue light application, indicating fast reversibility (Figures 1D–1F; Video S1). In addition to SspB-mCh-p60, a construct containing the higher affinity $SspB_{nano}$ instead of $SspB_{micro}$ was also tested but showed undesirable dark-state activity and microtubule localization prior to activation.

In order to confirm that microtubules were locally disassembled, local opto-katanin-mediated microtubule severing was performed, and cells were subsequently fixed and stained for α-tubulin (Figure 1G). Severing appears highly localized, suggesting that p60-mediated severing does not trigger persistent microtubule shrinkage, consistent with *in vitro* work showing that katanin-mediated severing leads to spontaneous incorporation of GTP-tubulin and increases microtubule rescues.[20] This contrasts with laser ablation-mediated microtubule severing that induces extensive microtubule depolymerization.[4] To test microtubule recovery after severing, we compared cells fixed directly after local severing (Figure 1H) with cells allowed to recover for 1 min after switching off local blue light illumination (Figure 1K). We chose to use RPE1 cells for this experiment due to their more substantial expression levels of CAMSAP2, a microtubule minus-end-binding protein, to see if microtubule severing would induce stable minus ends. Cells fixed immediately after illumination consistently showed an absence of microtubules within the ROI and occasionally some CAMSAP2-decorated minus ends (Figures 1I and 1J, white arrows). Cells fixed 1 min after stopping the illumination displayed very strong recovery of microtubules inside the ROI and no striking increase in CAMSAP2 stretches (Figures 1L–1N). We also attempted to quantify recovery dynamics in live cells using the lowest usable concentration of the far red silicone-rhodamine (SiR)-labeled microtubule probe, SiR-tubulin, thus minimizing its microtubule stabilizing activity. As expected, we saw that the loss of SspB-mCh-p60 from the ROI after activation correlated with a steep decrease in SiR-tubulin intensity indicative of microtubule severing (Figures S1A–S1C; Video S2). While after 1 min of recovery it was possible to see some dimly SiR-tubulin-labeled microtubule ends inside the ROI (white arrows, Figure S1A), SiR-tubulin intensity did not show full recovery inside the severed area, even after 17.5 min (Figure S1B). This can be attributed, at least in part, to the preference of SiR-tubulin for more long-lived microtubules,[21] likely due to its slow on rate. It is also possible that despite efforts to minimize SiR-tubulin-induced microtubule stabilization, there was still some stabilizing effect that delayed recovery.[22,23]

Opto-katanin-mediated microtubule disassembly with different microtubule anchors

We next investigated what properties made a good anchor for the opto-katanin tool by testing several different MAPs (Table 1). Various microtubule anchors were tested in live cells co-transfected with SspB-mCh-p60, assessed in live-cell imaging experiments and scored for microtubule binding, bundling, and severing (Figure S2; Table 1). From the anchors tested, it was apparent that microtubule bundling activity, such as observed for MAP7, Tau, and MAP2C, was generally predictive of poor microtubule-severing activity, even though these anchors could recruit katanin (Figure S2; Table 1). The observation that the MAP7 fragments missing the C-terminal domain did not bundle microtubules and performed well as microtubule-severing anchors (Table 1) further supports the notion that microtubule bundling inhibits opto-katanin-mediated severing. As to be expected, the absence of microtubule binding was also a good predictor of poor severing activity due to poor recruitment of SspB-mCh-p60 to microtubules (Figure S2; Table 1). We found that the addition of mCl3-iLID could reduce microtubule-binding affinity or even abrogate microtubule binding (Table 1). Some constructs containing previously identified microtubule-binding domains showed poorer microtubule localization, compared with the full-length constructs, for example, MAP7D3, Tau,[24] and MAP2C[25] (Table 1). This implies that additional protein domains contribute to microtubule binding. Indeed, previous work has suggested that in addition to the major N-terminal microtubule-binding domain, MAP7D3 also contains a region with microtubule affinity in its C terminus.[26,27] Similarly, the 4R microtubule-binding domain of Tau has previously been shown to have a 25-fold reduced microtubule-binding affinity, compared with full-length Tau.[24]

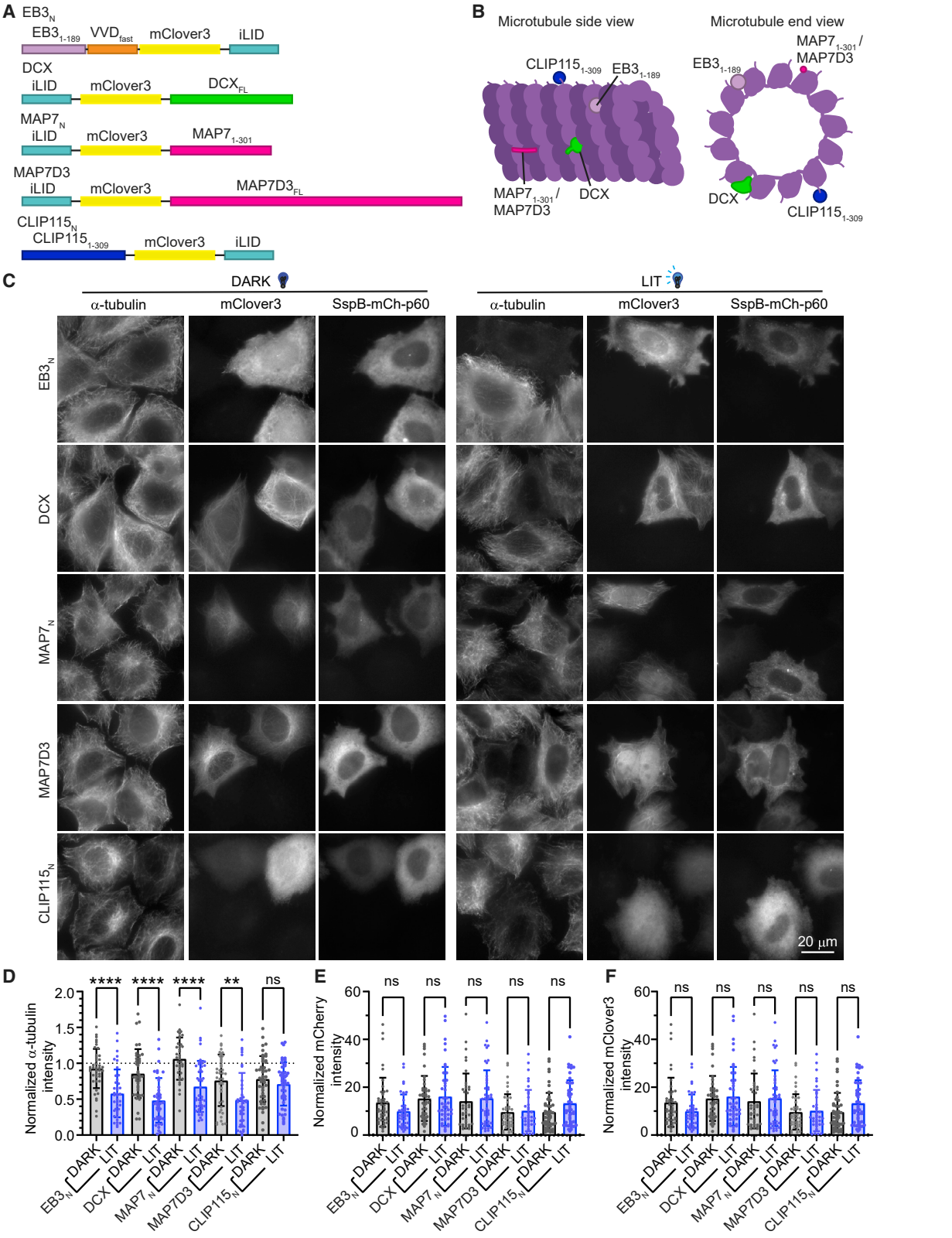

Figure 2. Use of different microtubule-binding domains to support opto-katanin-mediated microtubule disassembly

(A) Overview of optogenetic microtubule anchor constructs.

(B) Scheme showing the position of microtubule-binding sites of $EB3_N$, DCX, $MAP7_N$/MAP7D3, and $CLIP115_N$ on the microtubule.

(legend continued on next page)

We then focused in more detail on the anchors that did trigger light-induced microtubule disassembly by SspB-mCh-p60. These included proteins with different microtubule-binding sites: $EB3_N$[28] and doublecortin (DCX)[29] that bind between protofilaments; $MAP7_N$[30] and MAP7D3, which straddle the inter-dimer and the intra-dimer tubulin interfaces; and the cytoskeleton-associated protein-glycine-rich (CAP-Gly) domain-containing $CLIP115_N$, which binds the tail of α-tubulin[31] (Figures 2A and 2B). Since excessive expression of constructs resulted in dark-state activation of microtubule cutting, a maximum threshold for the expression of microtubule anchors and SspB-mCh-p60 was imposed. After whole-cell blue light activation (LIT), all five anchor constructs combined with SspB-mCh-p60 could induce microtubule depolymerization that was visualized by staining with anti-α-tubulin antibodies (Figures 2C and 2D). As a control, we confirmed that anchor constructs alone did not induce microtubule disassembly or reduce α-tubulin staining by blocking the antibody epitope (Figures S3A and S3B). Certain anchors combined with SspB-mCh-p60 had a higher dark-state activity than others; in particular, the $CLIP115_N$ and the MAP7D3 anchors showed a large decrease in α-tubulin staining without light activation (Figure 2D). $EB3_N$ and $MAP7_N$ anchors showed the lowest dark-state activation (Figure 2D). We confirmed that the anchor and SspB-mCh-p60 expression was comparable for all conditions (Figures 2E and 2F), and therefore differences in microtubule density observed between DARK and LIT conditions for each anchor could be attributed to its ability to recruit and activate katanin. Altogether, our data suggest that a good microtubule anchor for opto-katanin should bind individual microtubules well but not bundle them and that a direct interaction with tubulin tails, like in $CLIP115_N$, may be disadvantageous in this system.

Since overexpressing any MAP is expected to affect microtubule dynamics, we characterized the impact of the best performing anchors on microtubule polymerization without construct activation. Cells were stained for EB1 + EB3 to assess growing microtubule tips. $EB3_N$ overexpression displaced native EB1 + EB3 from the plus ends; $MAP7_N$ showed comparable EB1 + EB3 comets, compared with untransfected cells; and DCX showed a reduction in EB1 + EB3 comets, compared with untransfected cells (Figure S3C). In order to visualize the impact of the displacement of native EB1 + EB3 in $EB3_N$-expressing cells, we stained for CLIP-170, a protein that requires EBs for its recruitment to microtubule plus ends. As expected, $EB3_N$-transfected cells showed a reduction but not a complete abrogation of CLIP-170 recruitment to plus ends (arrows, Figure S3D). Next, microtubule dynamics were observed and quantified in live cells either overexpressing mCh-CLIP-170 alone or together with $MAP7_N$, $EB3_N$,or $EB3_N$ + SspB-mCh-p60. Since mCh-CLIP-170 was more poorly recruited in the $EB3_N$- and EB3N + SspB-mCh-p60-expressing cells, the $EB3_N$-VVD-Halo-iLID was visualized to track plus ends in these cells instead. We saw a small decrease in growth velocity and catastrophe frequency with $MAP7_N$ (Figures S3E–S3G), consistent with the notion that $MAP7_N$ stabilizes microtubules. $EB3_N$ combined with SspB-mCh-p60 had a slightly higher growth velocity, and $EB3_N$ and $EB3_N$ + SspB-mCh-p60 also displayed a mild increase in catastrophe frequency (Figures S3E–S3G), consistent with the fact that full-length EB1 and EB3 suppress catastrophes.[19]

Since the $EB3_N$ anchor exhibited the least dark-state activity and the greatest difference between DARK and LIT conditions, as well as only a minor impact on microtubule dynamics, this construct was used for subsequent experiments.

Application of opto-katanin to locally block microtubule-based transport

Next, we set out to test the capacity of opto-katanin to locally disrupt microtubule functions, such as their ability to serve as tracks for transport. Among all cell types, neurons have the most elaborate and specialized transport network, which consists of a large population of stabilized microtubules bearing numerous posttranslational modifications and decorated with a great diversity of MAPs. Given that a highly stablized microtubule network may be difficult to disassemble, we first set out to test whether opto-katanin could sever microtubules in protrusions of differentiated day *in vitro* 9 (DIV9) neurons. Differentiated neurons were transiently transfected with opto-katanin constructs at DIV7 and used for live-cell experiments 2 days later, when neurites were locally pulsed with blue light to induce microtubule severing (Figure 3A). We found that microtubules could be severed in neurites within approximately 10 min, as observed by SiR-tubulin labeling and the rise and fall of SspB-mCh-p60 intensity (Figures 3B–3D; Video S3). To confirm efficient microtubule severing, we performed antibody staining, which in cultures of differentiated neurons is complicated by the presence of axons from neighboring neurons, recognizable by their dense and strongly acetylated microtubule bundles (Figures 3E–3H). Nevertheless, we observed severing of both acetylated and tyrosinated microtubule populations in the neurites and cell body of fully illuminated or locally illuminated neurons (Figures 3E–3G). Locally illuminated neurons stained for α-tubulin also showed microtubule loss inside the ROI, indicating that all microtubule populations are severed (blue arrows, Figure 3H).

In order to test the impact of microtubule severing on transport, we observed late endosome and lysosome (endolysosome) motility in DIV9 neurons using a LAMP1-HaloTag (LAMP1-Halo) probe. This traps any cargoes present at the cut site (blue arrow, Figures 3I–3L; Videos S4 and S5). In some cases, local microtubule severing could cause endolysosome traffic jams (Figures 3I and 3J; orange arrows, Video S4), whereas in other cases it resulted in rerouting of endolysosomes to other neurites (Figures 3K and 3L; Video S5). As expected, the number of motile late endolysosomes also dropped in the ROI after microtubule

(C–F) HeLa cells were co-transfected with SspB-mCh-p60 and microtubule anchor constructs shown in (A) and (B) and either fixed in the dark (DARK) or fixed after a 16 min incubation under blue light (LIT), prior to immunostaining for α-tubulin and imaging on a widefield microscope. In (C), representative images are shown. (D)–(F) show quantification of normalized fluorescence intensity of α-tubulin immunostaining (D), mCherry intensity to indicate SspB-mCh-p60 expression (E), or mClover3 intensity to indicate microtubule anchor construct expression (F). In (D)–(F), n = 40–47 cells across 3 independent experiments, and plots indicate mean ± SD with individual cell measurements shown as dot points. ns, not significant, $^{**}p < 0.01$ and $^{****}p < 0.0001$.
See also Table 1 and Figure S3.

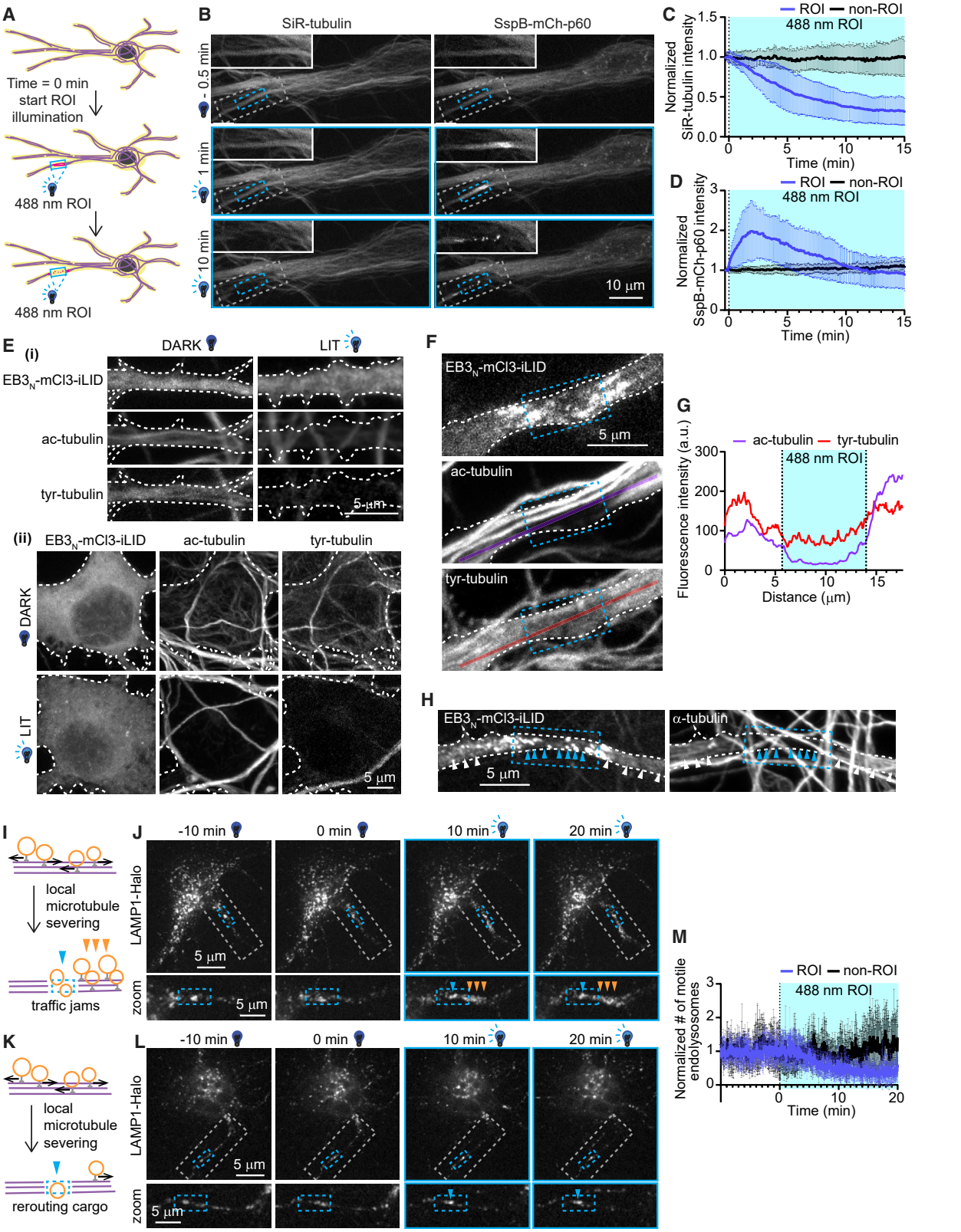

(legend on next page)

disassembly (Figure 3M). Similarly, localized microtubule severing could also be used to block transport of exocytic Halo-Rab6A-labeled vesicles in U2OS cells, where the vesicles paused near the microtubule cut site and then moved away along remaining microtubules (arrows, Video S6). This suggests that transport of cargoes is an adaptive process and that cargoes can be redirected if necessary, and opto-katanin is a suitable tool to perturb and study such processes.

Application of opto-katanin to study ER tubule formation and maintenance

Aside from facilitating long-range transport, microtubules are also important regulators of the morphology of different organelles, such as the endoplasmic reticulum (ER). While *in vitro* ER does not require microtubules to form tubular structures,[32] *in vivo* microtubules are thought to be important regulators of ER tubules, since nocodazole-mediated microtubule disassembly results in a dramatic shift from ER tubules to sheets.[33,34] The mechanism by which microtubules maintain ER tubules is still unclear. Microtubules are known to be required for the formation of ER tubules in mammalian cells by motor-based sliding or ER attachment to growing microtubule tips.[35–37] Using Halo-KDEL to visualize ER (Figure 4A), we observed that after formation; ER tubules either persisted or underwent lateral movement and collapsed within a few seconds (Figure 4B, arrows). We chose to locally disassemble microtubules in an area in the middle of cytoplasm to maintain a border of microtubules at the periphery where new ER tubules could be generated and ER could be anchored (Figure 4C). Opto-katanin enabled localized microtubule clearance in COS-7 cells in 1.5 min, and the area was maintained devoid of microtubules by continuing to activate opto-katanin within the ROI (Figure 4D; Video S7). Interestingly, local disassembly of microtubules resulted in an immediate local inhibition of ER dynamics and an acute drop in ER density but no conversion of ER tubules to sheets or ER loss, not even over a longer timescale of 20 min (Figures 4D–4H; Video S7). These data suggest that microtubules are not necessary to directly stabilize ER tubules and that ER tubules and three-way junctions between them can be stable without microtubule anchoring within large gaps between microtubules. Inside the area depleted of microtubules, there was no ER tubulation and very few events of lateral movement and collapse of existing tubules; also, the lateral movements that were observed occurred over timescales of minutes rather than seconds (Figure 4I). This suggests that microtubules are not necessary to facilitate lateral displacement of ER tubules; however, since such events are typically observed promptly after ER tubulation (Figure 4B), they are likely primarily driven by local ER remodeling directly following tubule extension. The remaining ER dynamics in a microtubule-depleted area consisted of slow drift toward the cell center, which was previously shown to be driven by actomyosin retrograde flow,[38] likely combined with Brownian motion and cytoplasmic diffusion.[39]

We also did not observe a conversion of ER tubules to sheets within larger ROIs if no sheets were present in the illuminated areas to begin with (Figure S4A). However, cells that already exhibited ER sheets within the ROI did form new and larger sheets after microtubule disassembly (white arrows, Figure S4B; Video S8). ER sheets inside areas cleared of microtubules moved to coalesce with other sheets (Figure S4C). Our observations suggest that when microtubules are locally depolymerized, the proportion of sheets and tubules is determined by abundance of ER shaping factors present in the cell area (Figure S4D). Altogether, our results support a model where ER tubule density and dynamics are underpinned by microtubule-mediated ER tubulation, but microtubule-ER interactions are not directly required for the maintenance of ER tubules.

Application of opto-katanin to perturb Golgi morphology and dynamics

Microtubules nucleated and anchored at the Golgi are used as tracks for vesicle transport.[2,40] Even though cells do not require microtubules for secretion,[41] cooperative microtubule motor-based transport is necessary for long-distance translocation of

Figure 3. Localized optogenetic microtubule severing in neurons blocking microtubule-based transport

All experiments used differentiated DIV9 rat hippocampal neurons transfected at DIV7 with $EB3_N$-VVD-mCl3-iLID and SspB-mCh-p60.

(A) Schematic of experiment: neurons with opto-katanin constructs were locally illuminated with blue light to induce local recruitment of opto-katanin constructs and microtubule severing.

(B–D) Neurons were stained with SiR-tubulin and pulsed locally with blue light at a ROI (marked by blue dashed box) from time = 0 min on a spinning disc microscope. (B) shows representative stills 0.5 min before (−0.5 min), 1 min after, and 10 min after starting blue light pulsing, see also Video S3. (C) and (D) show quantification of normalized fluorescence intensity inside blue light pulsed region (ROI) and a comparable region in the same cell not illuminated with blue light (non-ROI) of SiR-tubulin (C) and SspB-mCh-p60 (D). Graphs indicate mean ± SD, n = 15–16 ROI from 8 neurons over 3 experiments.

(E) Neurons were either fixed in the dark (DARK) or illuminated with blue light for 16 min prior to fixation (LIT) and stained for tyrosinated tubulin (tyr-tubulin) and acetylated tubulin (ac-tubulin). Panels show maximum intensity projections of (i) neurite and (ii) cell body.

(F–H) Neurons were locally pulsed with blue light inside ROI (indicated by blue dashed box), fixed without recovery, stained for ac-tubulin and tyr-tubulin (F and G) or α-tubulin (H), and imaged on an Airyscan confocal microscope. (F) and (H) show maximum intensity projections at the site of local microtubule severing with transfected cell outlined by white dashed line. Line scans over site of microtubule severing from (F), with ac-tubulin signal shown in purple and tyr-tubulin signal shown in red (G); and white arrows highlight uncut microtubules outside ROI and blue arrows show area cleared of microtubules in transfected cell (H).

(I and K) Experiment schemes: local microtubule severing inside a ROI (shown with blue dashed box) perturbs endolysosome (orange circles) trafficking by trapping them inside ROI (blue arrow) and in some cases causing traffic jams (orange arrows) (I) and in other cases causing rerouting of cargo to other neurites (K).

(J, L, and M) Neurons also co-transfected at DIV7 with LAMP1-Halo to label endolysosomes were pulsed locally with blue light (marked by blue dashed box) from 0 min onward on a spinning disc microscope. (J) shows the still images of an instance in which a traffic jam (highlighted by orange arrows) was generated by localized microtubule severing, along with trapped cargoes at the site of microtubule severing (blue arrow), see also Video S4. (L) shows the still images of an instance where endolysosomes were rerouted away from the neurite in which local microtubule severing was performed, and blue arrow indicates cargo trapping at the site of local microtubule severing, see also Video S5. (M) shows quantification of motile endolysosomes inside ROI and a comparable region not pulsed by blue light (non-ROI); graph shows mean ± SD, n = 5 ROI from 4 neurons over 3 experiments.

See also Videos S3, S4, S5, and S6.

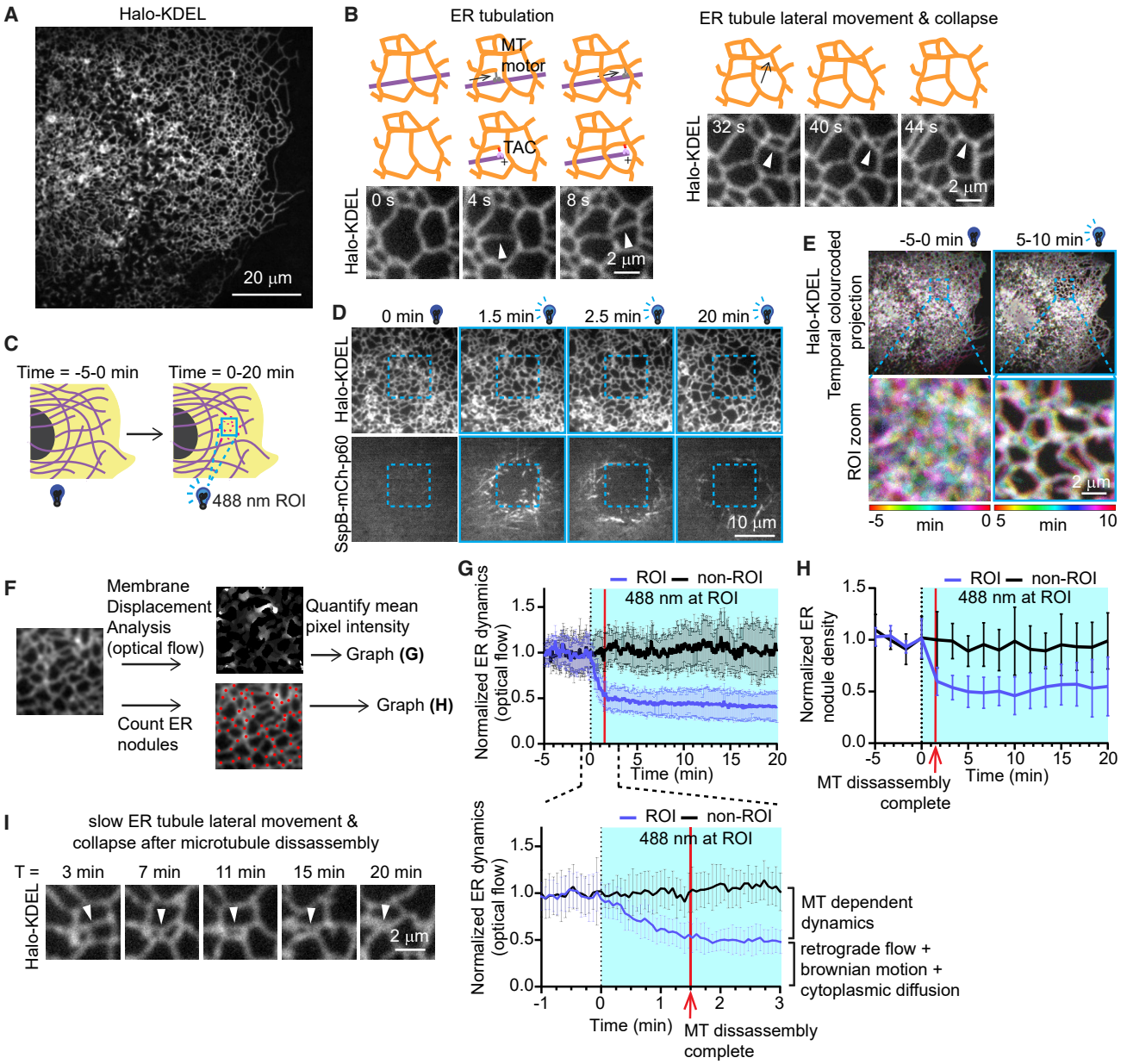

Figure 4. Localized optogenetic microtubule disassembly to study microtubule dependence of ER morphology and dynamics

(A–I) COS-7 co-expressing $EB3_N$-VVD-mCl3-iLID, SspB-mCh-p60, and Halo-KDEL as an ER marker. In (B), ER tubules are generated by two mechanisms, ER coupling to microtubule (MT) motors moving along a microtubule and ER coupling to growing microtubule tips via tip associated complexes (TAC). After generation of a new ER tubule the tubule will either persist for some time or undergo lateral movement and collapse. (C) indicates scheme of the experimental setup: microtubules were optogenetically severed in a central cytoplasmic region using localized pulses of blue light inside a ROI (marked by blue dashed box) from 0 min onward. (D) shows ER at and around site of local microtubule severing; Halo-KDEL and SspB-mCh-p60 with ROI marked by a blue dashed box before local blue light illumination (0 min) and 1.5, 2.5, and 20 min after starting blue light illumination at ROI, see also Video S7. In (E), Z projections of Halo-KDEL frames are color coded for time before (−5 to 0 min) and after (5–10 min) local microtubule severing. (F) indicates the scheme of the analysis pipeline: membrane displacement was analyzed in ROI and non-ROI regions using optical flow membrane displacement analysis that converts movement into pixel intensity, and then mean pixel intensity was quantified. ER nodules (marked by red dots) were also counted in ROI and non-ROI regions. (G) and (H) show the quantification of normalized ER dynamics (G) and normalized number of ER nodules (H), analyzed as illustrated in panel (F); graphs show mean ± SD, n = 16 cells across 4 independent experiments. Red line indicates time at which MTs have been locally disassembled inside ROI. (I) indicates slow ER tubule lateral movement and collapse inside area where microtubules were locally disassembled.

See also Figure S4 and Videos S7 and S8.

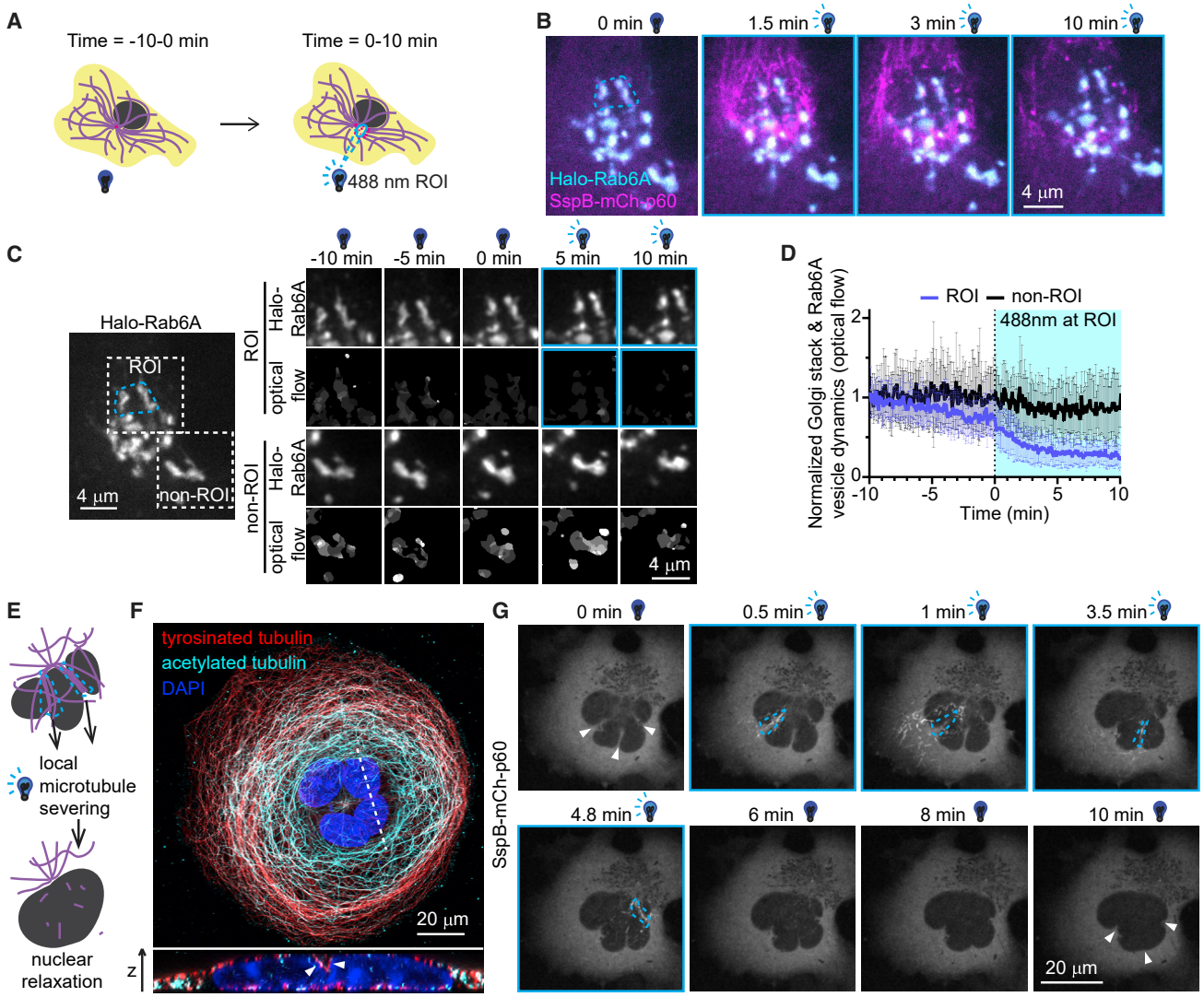

Figure 5. Localized optogenetic microtubule severing to perturb Golgi and nuclear morphology and dynamics

(A–D) U2OS co-expressing EB3$_N$-VVD-mCl3-iLID, SspB-mCh-p60, and Halo-Rab6A to label Golgi and exocytic vesicles. (A) indicates the scheme of the experimental setup: ROI (marked by blue dashed box) was drawn around a subset of the Golgi stacks and pulsed with blue light from 0 min onward to locally sever microtubules. (B) shows local microtubule severing at Golgi; Halo-Rab6a (cyan) and SspB-mCh-p60 (magenta) with ROI marked by a blue dashed box before local illumination (0 min) and 1.5, 3, and 10 min after starting blue light illumination at ROI, see also Video S9. (C) indicates the dynamics of Halo-Rab6A-labeled Golgi membranes; images show zoomed stills of Halo-Rab6A and the corresponding optical flow analysis (as illustrated in Figure 4F) in ROI and non-ROI regions before (−10, −5, and 0 min) and after (5 and 10 min) local microtubule severing in ROI (marked by blue dashed box). In (D), normalized dynamics of Halo-Rab6A-labeled membranes are analyzed by optical flow; graph shows mean ± SD, n = 14 cells from 3 independent experiments.

(E) Scheme of the experimental setup: COS-7 with lobulated nuclei were pulsed with blue light sequentially within areas showing nuclear invaginations to sever microtubule bundles around the nucleus.

(F) Fixed COS-7 cell with a lobulated nucleus, stained for DAPI (dark blue), acetylated tubulin (cyan), and tyrosinated tubulin (red), showing microtubules inside nuclear invaginations (arrowheads).

(G) COS-7 cell co-expressing EB3$_N$-VVD-mCl3-iLID and SspB-mCh-p60 with a lobulated nucleus was exposed to blue light in ROIs shown in dashed blue lines to sequentially sever microtubule bundles, see also Video S10. After microtubule bundle severing, gradual nuclear relaxation was observed; arrows indicate locations of nuclear invaginations that were present prior to microtubule severing.

See also Videos S9 and S10.

secretory cargo.[42] Upon total microtubule disassembly using nocodazole, the Golgi becomes fragmented and dispersed; however, the process by which this occurs is complicated and not fully understood.[43] Furthermore, dynein has been implicated in the localization and compacting of the Golgi near the centrosome.[44] In order to investigate the dependence of Golgi positioning and morphology on microtubules, we disassembled microtubules around a subset of (Rab6A-labeled) Golgi stacks (Figures 5A and 5B). Interestingly, the positioning of these stacks was not altered, compared with the Golgi stacks in a region that was not illuminated with blue light (Figures 5B and 5C; Video S9). However, an analysis of membrane dynamics (Figure 4F)

revealed a strong reduction of Golgi stack and Rab6A vesicle motility upon microtubule disassembly (Figure 5D). This quantification indicates a decrease in lateral movement and transport and does not rule out secretion of vesicles directly under the Golgi, as observed in kinesin knockout studies.[42] Local microtubule disassembly also resulted in a local loss of Rab6A-positive Golgi tubules (arrows, Video S9), supporting the idea that such tubules are formed by kinesin-1-mediated membrane pulling.[45] Our results indicate that at least on shorter timescales (10 min), the Golgi ribbon morphology and membrane tubulation, but not Golgi positioning, are affected by microtubule disassembly. Our results support the idea that disorganization of the microtubule network during nocodazole-mediated disassembly combined with the activity of molecular motors contributes to Golgi fragmentation in such experiments.[43] It is possible that longer microtubule perturbations would be necessary to see some effect on Golgi positioning using our experimental system.

Application of opto-katanin to investigate microtubule-mediated nuclear constriction

Microtubules can also participate in shaping the nucleus: in myeloid progenitors, microtubule bundles deforming the nucleus have been reported to influence chromatin organization and gene expression to drive differentiation.[3] Microtubule-mediated nuclear constriction and formation of lobulated nuclei have also been observed in cancer cell lines and untransformed epithelial cells.[46,47] We observed lobulated nuclei in a subpopulation of COS-7 cells and tested whether it was possible to use opto-katanin to probe the biophysical forces induced by the microtubule bundles around these nuclei (Figure 5E). Immunostaining revealed that these microtubule bundles contained both tyrosinated and acetylated microtubules (Figure 5F). We used opto-katanin to sequentially sever perinuclear microtubule bundles and observed slow sequential relaxation of nuclear invaginations, taking between 3 and 7 min after microtubule bundle severing (Figure 5G; Video S10). This suggests that, in contrast to the plastic deformation of nuclei in myeloid progenitors,[3] microtubules were imposing constricting forces causing elastic deformation of COS-7 nuclei, which recovered a rounded shape after microtubule belts were cut. Furthermore, as observed in neurites, the opto-katanin tool could be applied to sever both acetylated and tyrosinated microtubules. These data further demonstrate that opto-katanin can be used to study forces locally exerted by microtubules on subcellular structures.

Effects of opto-katanin on cell division

Since opto-katanin could effectively disrupt microtubules in interphase cells, we wanted to test whether it could also be used to sever microtubules during mitosis. To achieve homogeneous expression levels of the two constructs within a dividing cell population, we generated a stable HT1080 cell line using a doxycycline (dox)-dependent regulatory system with an optimized transcription factor rtTA2^{S}-m2[48] (Figure 6A). In this cell line, only dox-treated cells (+dox) expressed the opto-katanin constructs (Figure 6B). We found that expression of opto-katanin constructs without light activation (DARK +dox) or blue light treatment alone (LIT 1 h −dox) did not prevent cells from undergoing mitosis; however, quantification of mitotic stages showed a larger proportion of cells in prometaphase and metaphase, compared with cells without light treatment or opto-katanin expression (DARK −dox; Figures 6C and 6D). This suggests that opto-katanin expression or light treatment alone can affect but not block mitotic progression. Cells expressing opto-katanin and treated with blue light were arrested in prometaphase and metaphase and had smaller and sparser spindles; however, spindles were rarely disassembled completely (Figures 6C and 6D). Similarly, when the dox-treated opto-katanin stable cell line was tested in a live-cell experiment, whole-cell blue light illumination resulted in a marked reduction of spindle size over a span of 15 min (Figure 6E). These results show that opto-katanin constructs do not block cell division without blue light illumination, indicating that the system can potentially be utilized for local spindle perturbations.

DISCUSSION

In this study, we have generated a potent tool for rapid, precise, and reversible microtubule disassembly. We were able to induce microtubule elimination using a variety of different engineered microtubule anchors, suggesting that regulation of katanin p60 recruitment is sufficient to control its microtubule-severing activity. We have demonstrated successful opto-katanin-mediated depletion of microtubule polymer from various cellular structures, including both dynamic, tyrosinated, and stable, acetylated microtubules. Profound microtubule disassembly in primary neurons is by itself an important achievement, because complete microtubule depolymerization in neurons using conventional tools such as the tubulin-sequestering drug nocodazole is difficult or impossible.[49] Further, we showed that the use of opto-katanin allows local removal of microtubules in sharply defined cell areas, while no major disruptions occur in the remaining microtubule network or in vesicle, ER, and Golgi dynamics outside the region of targeted microtubule disassembly. This highly localized action is possible because katanin-severed microtubule ends remain relatively stable. This distinguishes opto-katanin from photoablation, which triggers strong depolymerization of severed microtubules and perturbs all structures in the illuminated cell volume,[4,5] and from photopharmacological tools for microtubule disassembly, which rapidly diffuse throughout the cell and are difficult or impossible to apply with subcellular precision.[50–52] Aside from being highly localized and more complete than nocodazole-driven microtubule disassembly, opto-katanin-mediated severing also occurs rapidly (1.5–10 min for opto-katanin versus 30 min or more for nocodazole), which allows for studying the results of local microtubule elimination on short timescales and using cell regions not illuminated with blue light as a control.

To illustrate the experimental applications of opto-katanin, we used localized microtubule disassembly to create obstacles for exocytic vesicles and endolysosomes and saw that their transport is an adaptive process and that cargoes can be moved in a different direction after pausing at a microtubule gap. We also found that microtubules are essential for generating new ER tubules and keeping them dynamic, that they are not directly required to stabilize ER tubules, and that microtubule-ER interactions in surrounding areas are sufficient to maintain an extensive tubular network in a region devoid of microtubules. Local microtubule disassembly could also trigger

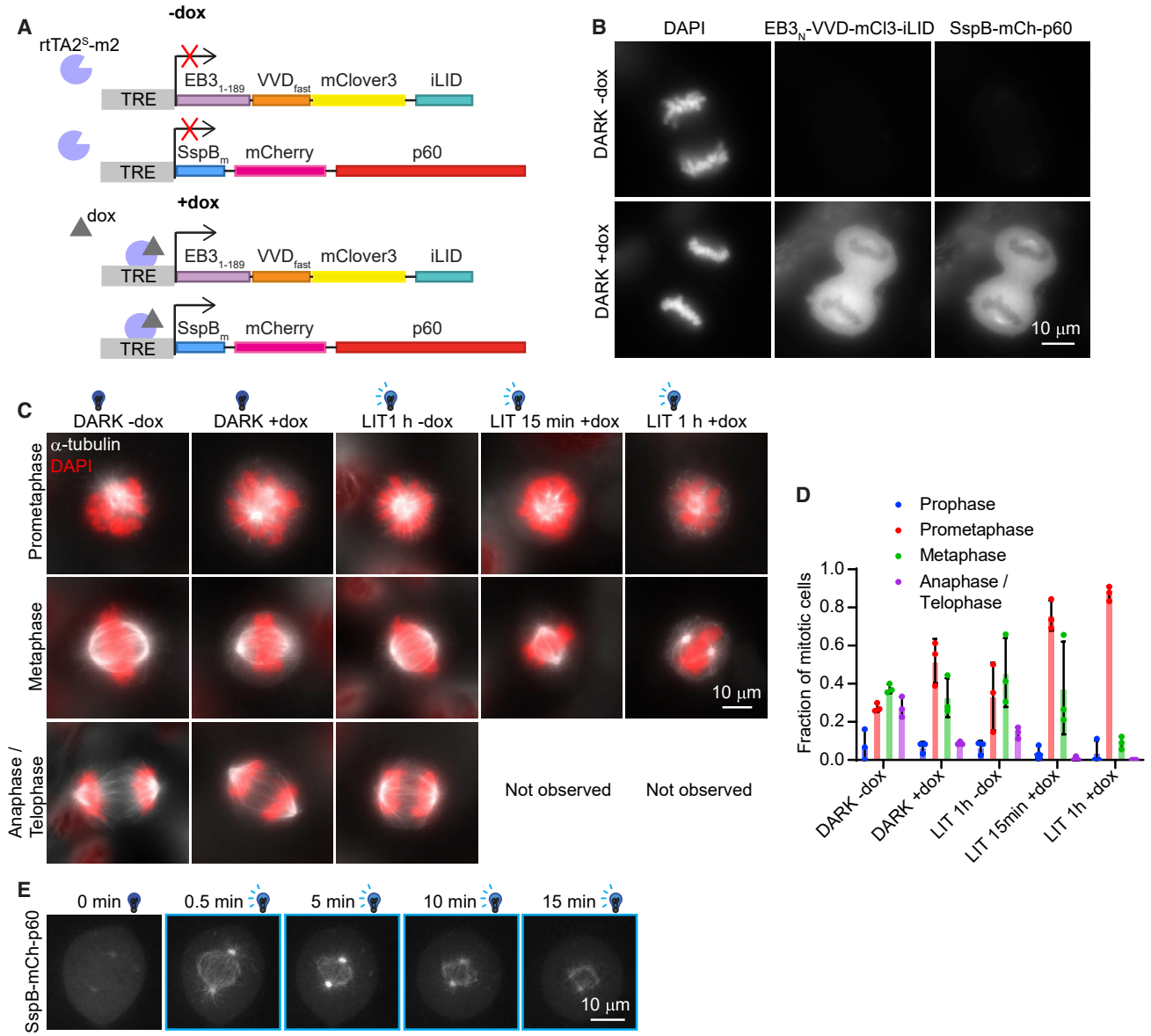

Figure 6. Generation of an opto-katanin stable HT1080 cell line for inducible mitotic arrest and spindle disassembly

(A) Schematic overview of opto-katanin constructs preceded by TRE-containing promoters, which can bind to the tetracycline/doxycycline-sensitive transcription factor rtTA2^S-m2. This results in transcription of opto-katanin constructs only after doxycycline addition (+dox) but not in its absence (−dox).

(B) Cells from stable cell line either treated +dox or −dox fixed in dark (DARK) conditions, stained for DAPI, and imaged on a widefield microscope.

(C and D) Cells treated +dox or −dox and either fixed in DARK conditions or after whole-cell blue light treatment (LIT) for 15 min or 1 h. In (C), representative cells are shown for prometaphase, metaphase, and anaphase/telophase. (D) shows the quantification of the fraction of mitotic cells in prophase, prometaphase, metaphase, and anaphase/telophase; graph shows mean ± SD with individual experimental values shown as dot points. n = 3 independent experiments with 30–55 cells analyzed per treatment group per experiment.

(E) +dox-treated mitotic cell imaged with field of view blue light activation from 0 min onward on a spinning disc microscope.

expansion of ER sheets, but only in cell regions where sheets were already present. Furthermore, we showed that Golgi dynamics and morphology can be manipulated with opto-katanin. Also, we demonstrated that microtubule constrictions of COS-7 cell nuclei can be individually severed, resulting in the nucleus slowly reassuming a rounded shape. Lastly, we presented a system for generating a stable cell line with opto-katanin constructs and showed that expression of opto-katanin constructs without blue light activation is not toxic for cells. Future work could use opto-katanin to study the functional importance of local ER dynamics or quantify the recoil of the nucleus after microtubule severing to understand its biophysical properties.

While preparing this study for publication, a similar inducible approach using another severing enzyme, spastin, was described,[53] exemplifying the demand for such a tool. In

that system, the authors used mutations disrupting spastin binding to microtubules and a FRB/FKPB chemical heterodimerization or CRY2/CIBN light-inducible dimerization system to make the recruitment of mutant spastin to microtubules inducible.[53] While most of that study focused on the temporal control of spastin using an FRB/FKPB system, it also showed that local light-induced microtubule disassembly could be achieved with the CRY2/CIBN-based system, although at a rate approximately 6 times slower than described in our study here (~9 min for spastin versus 1.5 min for opto-katanin). Further work will be needed for side-by-side comparison of the two systems, their dark-state activity, and off-target effects.

Future work may be done to generate a severing tool specific to microtubule subpopulations. In designing the CAP-Gly domain CLIP115$_N$ anchor, we attempted to make a tool to specifically disassemble tyrosinated microtubules. While the CLIP115$_N$ anchor unfortunately had a high dark-state activity and failed to show a good light-induced microtubule-severing response, additional MAPs or nanobodies specific for posttranslational modifications exist that could be explored as potential microtubule anchors.[54] Indeed, FRB/FKPB-dependent spastin recruitment and microtubule severing could be induced by anchoring it with an antibody specific for tyrosinated tubulin, although it was not demonstrated that such a treatment leaves detyrosinated microtubules intact.[53]

We believe that opto-katanin is a strong asset for studying the functions of the microtubule cytoskeleton, since it is capable of performing precise, fast, and reversible microtubule-specific manipulations that were previously impossible. The tool shows no strong toxicity in the absence of blue light, and the use of an inducible expression system allows its stable maintenance within a cell population. The potential research applications of opto-katanin include determining the load-bearing contribution of microtubules in epithelial cell morphology,[55] muscle contraction,[56] nuclear positioning,[57] and migration through soft substrates;[58] studying microtubule orientation and assembly in neurites;[59] investigating reversible perturbation of specific microtubule nucleation sites; and elucidating the contribution of microtubules to various developmental morphogenetic processes.

STAR★METHODS

Detailed methods are provided in the online version of this paper and include the following:

- KEY RESOURCES TABLE
- RESOURCE AVAILABILITY
  - Lead contact
  - Materials availability
  - Data and code availability
- EXPERIMENTAL MODEL AND SUBJECT DETAILS
  - Cultured cells
  - Rats
- METHOD DETAILS
  - DNA constructs
  - Cell transfection
  - Rat neuron isolation and culture
  - Neuron transfection
  - HaloTag labeling
  - Lentivirus production
  - Cell line transduction and selection
  - Microscopy
- QUANTIFICATION AND STATISTICAL ANALYSIS
  - Fluorescence intensity measurement and normalization
  - Microtubule dynamics analysis
  - Dynamic lysosome analysis
  - Membrane dynamics analysis
  - ER nodule counting
  - Mitotic stage analysis
  - Statistical analysis

SUPPLEMENTAL INFORMATION

Supplemental information can be found online at https://doi.org/10.1016/j.cub.2022.09.010.

ACKNOWLEDGMENTS

The authors would like to acknowledge the following individuals: I. Smal for sharing and troubleshooting the use of the MtrackJ plugin, L.M. Voortman for sharing and troubleshooting the use of the membrane displacement analysis macro, P.J. Hooikaas for advising on MAP7 constructs, R.J. McKenney for advising on Tau constructs, E.A. Katrukha for advising on lysosome dynamics analysis, and M. Siemons for advising on laser power calculations. J.C.M.M. was supported by an EMBO long-term fellowship ALTF 261-2019, and A.A. was supported by ZonMW top grant 91216006.

AUTHOR CONTRIBUTIONS

Conceptualization, J.C.M.M. and A.A.; methodology, J.C.M.M.; investigation, J.C.M.M. and I.G.; writing – original draft, J.C.M.M. and A.A.; writing – review & editing, J.C.M.M. and A.A.; funding acquisition, J.C.M.M. and A.A.; resources, W.N., L.C.K., and A.A.; supervision, A.A., W.N., and L.C.K.

DECLARATION OF INTERESTS

The authors declare no competing interests.

Received: February 15, 2022
Revised: August 1, 2022
Accepted: September 6, 2022
Published: September 28, 2022

REFERENCES

1. Gudimchuk, N.B., and McIntosh, J.R. (2021). Regulation of microtubule dynamics, mechanics and function through the growing tip. Nat. Rev. Mol. Cell Biol. *22*, 777–795.
2. Hao, H., Niu, J., Xue, B., Su, Q.P., Liu, M., Yang, J., Qin, J., Zhao, S., Wu, C., and Sun, Y. (2020). Golgi-associated microtubules are fast cargo tracks and required for persistent cell migration. EMBO Rep. *21*, e48385.
3. Biedzinski, S., Agsu, G., Vianay, B., Delord, M., Blanchoin, L., Larghero, J., Faivre, L., Théry, M., and Brunet, S. (2020). Microtubules control nuclear shape and gene expression during early stages of hematopoietic differentiation. EMBO J. *39*, e103957.
4. Botvinick, E.L., Venugopalan, V., Shah, J.V., Liaw, L.H., and Berns, M.W. (2004). Controlled ablation of microtubules using a picosecond laser. Biophys. J. *87*, 4203–4212.
5. Khodjakov, A., Cole, R.W., and Rieder, C.L. (1997). A synergy of technologies: combining laser microsurgery with green fluorescent protein tagging. Cell Motil. Cytoskeleton *38*, 311–317.

6. van Haren, J., Charafeddine, R.A., Ettinger, A., Wang, H., Hahn, K.M., and Wittmann, T. (2018). Local control of intracellular microtubule dynamics by EB1 photodissociation. Nat. Cell Biol. *20*, 252–261.

7. Guntas, G., Hallett, R.A., Zimmerman, S.P., Williams, T., Yumerefendi, H., Bear, J.E., and Kuhlman, B. (2015). Engineering an improved light-induced dimer (iLID) for controlling the localization and activity of signaling proteins. Proc. Natl. Acad. Sci. USA *112*, 112–117.

8. Lu, W., Lakonishok, M., Liu, R., Billington, N., Rich, A., Glotzer, M., Sellers, J.R., and Gelfand, V.I. (2020). Competition between kinesin-1 and myosin-V defines *Drosophila* posterior determination. eLife *9*, e54216.

9. Ogawa, T., Nitta, R., Okada, Y., and Hirokawa, N. (2004). A common mechanism for microtubule destabilizers-M type kinesins stabilize curling of the protofilament using the class-specific neck and loops. Cell *116*, 591–602.

10. Hartman, J.J., Mahr, J., McNally, K., Okawa, K., Iwamatsu, A., Thomas, S., Cheesman, S., Heuser, J., Vale, R.D., and McNally, F.J. (1998). Katanin, a microtubule-severing protein, is a novel AAA ATPase that targets to the centrosome using a WD40-containing subunit. Cell *93*, 277–287.

11. McNally, F.J., and Vale, R.D. (1993). Identification of katanin, an ATPase that severs and disassembles stable microtubules. Cell *75*, 419–429.

12. Rezabkova, L., Jiang, K., Capitani, G., Prota, A.E., Akhmanova, A., Steinmetz, M.O., and Kammerer, R.A. (2017). Structural basis of katanin p60:p80 complex formation. Sci. Rep. *7*, 14893.

13. Zehr, E.A., Szyk, A., Szczesna, E., and Roll-Mecak, A. (2020). Katanin grips the beta-tubulin tail through an electropositive double spiral to sever microtubules. Dev. Cell *52*, 118–131.e6.

14. Faltova, L., Jiang, K., Frey, D., Wu, Y., Capitani, G., Prota, A.E., Akhmanova, A., Steinmetz, M.O., and Kammerer, R.A. (2019). Crystal structure of a heterotetrameric katanin p60:p80 complex. Structure *27*, 1375–1383.e3.

15. Jiang, K., Rezabkova, L., Hua, S., Liu, Q., Capitani, G., Altelaar, A.F.M., Heck, A.J.R., Kammerer, R.A., Steinmetz, M.O., and Akhmanova, A. (2017). Microtubule minus-end regulation at spindle poles by an ASPM-katanin complex. Nat. Cell Biol. *19*, 480–492.

16. Jiang, K., Faltova, L., Hua, S., Capitani, G., Prota, A.E., Landgraf, C., Volkmer, R., Kammerer, R.A., Steinmetz, M.O., and Akhmanova, A. (2018). Structural basis of formation of the microtubule minus-end-regulating CAMSAP-katanin complex. Structure *26*, 375–382.e4.

17. Nijenhuis, W., van Grinsven, M.M.P., and Kapitein, L.C. (2020). An optimized toolbox for the optogenetic control of intracellular transport. J. Cell Biol. *219*, e201907149.

18. Slep, K.C., and Vale, R.D. (2007). Structural basis of microtubule plus end tracking by XMAP215, CLIP-170, and EB1. Mol. Cell *27*, 976–991.

19. Komarova, Y., De Groot, C.O., Grigoriev, I., Gouveia, S.M., Munteanu, E.L., Schober, J.M., Honnappa, S., Buey, R.M., Hoogenraad, C.C., Dogterom, M., et al. (2009). Mammalian end binding proteins control persistent microtubule growth. J. Cell Biol. *184*, 691–706.

20. Vemu, A., Szczesna, E., Zehr, E.A., Spector, J.O., Grigorieff, N., Deaconescu, A.M., and Roll-Mecak, A. (2018). Severing enzymes amplify microtubule arrays through lattice GTP-tubulin incorporation. Science *361*. eaau1504.

21. David, A.F., Roudot, P., Legant, W.R., Betzig, E., Danuser, G., and Gerlich, D.W. (2019). Augmin accumulation on long-lived microtubules drives amplification and kinetochore-directed growth. J. Cell Biol. *218*, 2150–2168.

22. Lukinavičius, G., Reymond, L., D'Este, E., Masharina, A., Göttfert, F., Ta, H., Güther, A., Fournier, M., Rizzo, S., Waldmann, H., et al. (2014). Fluorogenic probes for live-cell imaging of the cytoskeleton. Nat. Methods *11*, 731–733.

23. Yan, Y., and Broadie, K. (2007). In vivo assay of presynaptic microtubule cytoskeleton dynamics in Drosophila. J. Neurosci. Methods *162*, 198–205.

24. Gustke, N., Trinczek, B., Biernat, J., Mandelkow, E.M., and Mandelkow, E. (1994). Domains of Tau protein and interactions with microtubules. Biochemistry *33*, 9511–9522.

25. Roger, B., Al-Bassam, J., Dehmelt, L., Milligan, R.A., and Halpain, S. (2004). MAP2c, but not tau, binds and bundles F-actin via its microtubule binding domain. Curr. Biol. *14*, 363–371.

26. Yadav, S., Verma, P.J., and Panda, D. (2014). C-terminal region of MAP7 domain containing protein 3 (MAP7D3) promotes microtubule polymerization by binding at the C-terminal tail of tubulin. PLoS One *9*, e99539.

27. Hooikaas, P.J., Martin, M., Mühlethaler, T., Kuijntjes, G.J., Peeters, C.A.E., Katrukha, E.A., Ferrari, L., Stucchi, R., Verhagen, D.G.F., van Riel, W.E., et al. (2019). MAP7 family proteins regulate kinesin-1 recruitment and activation. J. Cell Biol. *218*, 1298–1318.

28. Maurer, S.P., Fourniol, F.J., Bohner, G., Moores, C.A., and Surrey, T. (2012). EBs recognize a nucleotide-dependent structural cap at growing microtubule ends. Cell *149*, 371–382.

29. Fourniol, F.J., Sindelar, C.V., Amigues, B., Clare, D.K., Thomas, G., Perderiset, M., Francis, F., Houdusse, A., and Moores, C.A. (2010). Template-free 13-protofilament microtubule-MAP assembly visualized at 8 A resolution. J. Cell Biol. *191*, 463–470.

30. Ferro, L.S., Fang, Q., Eshun-Wilson, L., Fernandes, J., Jack, A., Farrell, D.P., Golcuk, M., Huijben, T., Costa, K., Gur, M., et al. (2022). Structural and functional insight into regulation of kinesin-1 by microtubule-associated protein MAP7. Science *375*, 326–331.

31. Weisbrich, A., Honnappa, S., Jaussi, R., Okhrimenko, O., Frey, D., Jelesarov, I., Akhmanova, A., and Steinmetz, M.O. (2007). Structure-function relationship of CAP-Gly domains. Nat. Struct. Mol. Biol. *14*, 959–967.

32. Dreier, L., and Rapoport, T.A. (2000). In vitro formation of the endoplasmic reticulum occurs independently of microtubules by a controlled fusion reaction. J. Cell Biol. *148*, 883–898.

33. Lu, L., Ladinsky, M.S., and Kirchhausen, T. (2009). Cisternal organization of the endoplasmic reticulum during mitosis. Mol. Biol. Cell *20*, 3471–3480.

34. Terasaki, M., Chen, L.B., and Fujiwara, K. (1986). Microtubules and the endoplasmic reticulum are highly interdependent structures. J. Cell Biol. *103*, 1557–1568.

35. Westrate, L.M., Lee, J.E., Prinz, W.A., and Voeltz, G.K. (2015). Form follows function: the importance of endoplasmic reticulum shape. Annu. Rev. Biochem. *84*, 791–811.

36. Waterman-Storer, C.M., and Salmon, E.D. (1998). Endoplasmic reticulum membrane tubules are distributed by microtubules in living cells using three distinct mechanisms. Curr. Biol. *8*, 798–806.

37. Bola, B., and Allan, V. (2009). How and why does the endoplasmic reticulum move? Biochem. Soc. Trans. *37*, 961–965.

38. Terasaki, M., and Reese, T.S. (1994). Interactions among endoplasmic reticulum, microtubules, and retrograde movements of the cell surface. Cell Motil. Cytoskeleton *29*, 291–300.

39. Brangwynne, C.P., Koenderink, G.H., MacKintosh, F.C., and Weitz, D.A. (2008). Cytoplasmic diffusion: molecular motors mix it up. J. Cell Biol. *183*, 583–587.

40. Wu, J., de Heus, C., Liu, Q., Bouchet, B.P., Noordstra, I., Jiang, K., Hua, S., Martin, M., Yang, C., Grigoriev, I., et al. (2016). Molecular pathway of microtubule organization at the Golgi apparatus. Dev. Cell *39*, 44–60.

41. Fourriere, L., Divoux, S., Roceri, M., Perez, F., and Boncompain, G. (2016). Microtubule-independent secretion requires functional maturation of Golgi elements. J. Cell Sci. *129*, 3238–3250.

42. Serra-Marques, A., Martin, M., Katrukha, E.A., Grigoriev, I., Peeters, C.A.E., Liu, Q., Hooikaas, P.J., Yao, Y., Solianova, V., Smal, I., et al. (2020). Concerted action of kinesins KIF5B and KIF13B promotes efficient secretory vesicle transport to microtubule plus ends. eLife *9*, e61302.

43. Minin, A.A. (1997). Dispersal of Golgi apparatus in nocodazole-treated fibroblasts is a kinesin-driven process. J. Cell Sci. *110*, 2495–2505.

44. Harada, A., Takei, Y., Kanai, Y., Tanaka, Y., Nonaka, S., and Hirokawa, N. (1998). Golgi vesiculation and lysosome dispersion in cells lacking cytoplasmic dynein. J. Cell Biol. *141*, 51–59.

45. Miserey-Lenkei, S., Chalancon, G., Bardin, S., Formstecher, E., Goud, B., and Echard, A. (2010). Rab and actomyosin-dependent fission of transport vesicles at the Golgi complex. Nat. Cell Biol. *12*, 645–654.

46. Chow, K.H., Factor, R.E., and Ullman, K.S. (2012). The nuclear envelope environment and its cancer connections. Nat. Rev. Cancer *12*, 196–209.

47. Wang, L., Paudyal, S.C., Kang, Y., Owa, M., Liang, F.X., Spektor, A., Knaut, H., Sánchez, I., and Dynlacht, B.D. (2022). Regulators of tubulin polyglutamylation control nuclear shape and cilium disassembly by balancing microtubule and actin assembly. Cell Res. *32*, 190–209.

48. Lamartina, S., Silvi, L., Roscilli, G., Casimiro, D., Simon, A.J., Davies, M.-E., Shiver, J.W., Rinaudo, C.D., Zampaglione, I., Fattori, E., et al. (2003). Construction of an rtTA2^{s}-m2/tts^{kid}-based transcription regulatory switch that displays no basal activity, good inducibility, and high responsiveness to doxycycline in mice and non-human primates. Mol. Ther. *7*, 271–280.

49. van de Willige, D., Hummel, J.J., Alkemade, C., Kahn, O.I., Au, F.K., Qi, R.Z., Dogterom, M., Koenderink, G.H., Hoogenraad, C.C., and Akhmanova, A. (2019). Cytolinker Gas2L1 regulates axon morphology through microtubule-modulated actin stabilization. EMBO Rep. *20*, e47732.

50. Thorn-Seshold, O., and Meiring, J.C.M. (2022). Photocontrolling microtubule dynamics with photoswitchable chemical reagents. Methods Mol. Biol. *2430*, 403–430.

51. Gao, L., Meiring, J.C.M., Kraus, Y., Wranik, M., Weinert, T., Pritzl, S.D., Bingham, R., Ntouliou, E., Jansen, K.I., Olieric, N., et al. (2021). A robust, GFP-orthogonal photoswitchable inhibitor scaffold extends optical control over the microtubule cytoskeleton. Cell Chem. Biol. *28*, 228–241.e6.

52. Müller-Deku, A., Meiring, J.C.M., Loy, K., Kraus, Y., Heise, C., Bingham, R., Jansen, K.I., Qu, X., Bartolini, F., Kapitein, L.C., et al. (2020). Photoswitchable paclitaxel-based microtubule stabilisers allow optical control over the microtubule cytoskeleton. Nat. Commun. *11*, 4640.

53. Liu, G.Y., Chen, S.-C., Lee, G.-H., Shaiv, K., Chen, P.-Y., Cheng, H., Hong, S.-R., Yang, W.-T., Huang, S.-H., Chang, Y.-C., et al. (2022). Precise control of microtubule disassembly in living cells. EMBO J. *41*, e110472.

54. Kesarwani, S., Lama, P., Chandra, A., Reddy, P.P., Jijumon, A.S., Bodakuntla, S., Rao, B.M., Janke, C., Das, R., and Sirajuddin, M. (2020). Genetically encoded live-cell sensor for tyrosinated microtubules. J. Cell Biol. *219*, e201912107.

55. Singh, A., Saha, T., Begemann, I., Ricker, A., Nüsse, H., Thorn-Seshold, O., Klingauf, J., Galic, M., and Matis, M. (2018). Polarized microtubule dynamics directs cell mechanics and coordinates forces during epithelial morphogenesis. Nat. Cell Biol. *20*, 1126–1133.

56. Robison, P., Caporizzo, M.A., Ahmadzadeh, H., Bogush, A.I., Chen, C.Y., Margulies, K.B., Shenoy, V.B., and Prosser, B.L. (2016). Detyrosinated microtubules buckle and bear load in contracting cardiomyocytes. Science *352*, aaf0659.

57. Zheng, Y., Buchwalter, R.A., Zheng, C., Wight, E.M., Chen, J.V., and Megraw, T.L. (2020). A perinuclear microtubule-organizing centre controls nuclear positioning and basement membrane secretion. Nat. Cell Biol. *22*, 297–309.

58. Bouchet, B.P., Noordstra, I., van Amersfoort, M., Katrukha, E.A., Ammon, Y.C., Ter Hoeve, N.D., Hodgson, L., Dogterom, M., Derksen, P.W.B., and Akhmanova, A. (2016). Mesenchymal cell invasion requires cooperative regulation of persistent microtubule growth by SLAIN2 and CLASP1. Dev. Cell *39*, 708–723.

59. Yau, K.W., Schätzle, P., Tortosa, E., Pagès, S., Holtmaat, A., Kapitein, L.C., and Hoogenraad, C.C. (2016). Dendrites in vitro and in vivo contain microtubules of opposite polarity and axon formation correlates with uniform plus-end-out microtubule orientation. J. Neurosci. *36*, 1071–1085.

60. Spits, M., Heesterbeek, I.T., Voortman, L.M., Akkermans, J.J., Wijdeven, R.H., Cabukusta, B., and Neefjes, J. (2021). Mobile late endosomes modulate peripheral endoplasmic reticulum network architecture. EMBO Rep. *22*, e50815.

61. Smal, I., Galjart, N., and Meijering, E. (2018). Accurate estimation of intracellular dynamics and underlying spatial structures using hierarchical trajectory smoothing. In 2018 IEEE 15th International Symposium on Biomedical Imaging (ISBI 2018), pp. 973–976.

62. Stepanova, T., Slemmer, J., Hoogenraad, C.C., Lansbergen, G., Dortland, B., De Zeeuw, C.I., Grosveld, F., van Cappellen, G., Akhmanova, A., and Galjart, N. (2003). Visualization of microtubule growth in cultured neurons via the use of EB3-GFP (end-binding protein 3-green fluorescent protein). J. Neurosci. *23*, 2655–2664.

63. Lu, M., and Kosik, K.S. (2001). Competition for microtubule-binding with dual expression of tau missense and splice isoforms. Mol. Biol. Cell *12*, 171–184.

64. Kapitein, L.C., Yau, K.W., Gouveia, S.M., van der Zwan, W.A., Wulf, P.S., Keijzer, N., Demmers, J., Jaworski, J., Akhmanova, A., and Hoogenraad, C.C. (2011). NMDA receptor activation suppresses microtubule growth and spine entry. J. Neurosci. *31*, 8194–8209.

65. Shin, E., Kashiwagi, Y., Kuriu, T., Iwasaki, H., Tanaka, T., Koizumi, H., Gleeson, J.G., and Okabe, S. (2013). Doublecortin-like kinase enhances dendritic remodelling and negatively regulates synapse maturation. Nat. Commun. *4*, 1440.

66. Hoogenraad, C.C., Akhmanova, A., Grosveld, F., De Zeeuw, C.I., and Galjart, N. (2000). Functional analysis of CLIP-115 and its binding to microtubules. J. Cell Sci. *113*, 2285–2297.

67. Falcón-Pérez, J.M., Nazarian, R., Sabatti, C., and Dell'Angelica, E.C. (2005). Distribution and dynamics of Lamp1-containing endocytic organelles in fibroblasts deficient in BLOC-3. J. Cell Sci. *118*, 5243–5255.

68. Matanis, T., Akhmanova, A., Wulf, P., Del Nery, E., Weide, T., Stepanova, T., Galjart, N., Grosveld, F., Goud, B., De Zeeuw, C.I., et al. (2002). Bicaudal-D regulates COPI-independent Golgi-ER transport by recruiting the dynein-dynactin motor complex. Nat. Cell Biol. *4*, 986–992.

69. Akhmanova, A., Hoogenraad, C.C., Drabek, K., Stepanova, T., Dortland, B., Verkerk, T., Vermeulen, W., Burgering, B.M., De Zeeuw, C.I., Grosveld, F., and Galjart, N. (2001). Clasps are CLIP-115 and -170 associating proteins involved in the regional regulation of microtubule dynamics in motile fibroblasts. Cell *104*, 923–935.

70. Noordstra, I., Liu, Q., Nijenhuis, W., Hua, S., Jiang, K., Baars, M., Remmelzwaal, S., Martin, M., Kapitein, L.C., and Akhmanova, A. (2016). Control of apico–basal epithelial polarity by the microtubule minus-end-binding protein CAMSAP3 and spectraplakin ACF7. J. Cell Sci. *129*, 4278–4288.

71. Kapitein, L.C., Yau, K.W., and Hoogenraad, C.C. (2010). Microtubule dynamics in dendritic spines. Methods Cell Biol. *97*, 111–132.

72. Lipka, J., Kapitein, L.C., Jaworski, J., and Hoogenraad, C.C. (2016). Microtubule-binding protein doublecortin-like kinase 1 (DCLK1) guides kinesin-3-mediated cargo transport to dendrites. EMBO J. *35*, 302–318.

73. Coquelle, F.M., Caspi, M., Cordelières, F.P., Dompierre, J.P., Dujardin, D.L., Koifman, C., Martin, P., Hoogenraad, C.C., Akhmanova, A., Galjart, N., et al. (2002). LIS1, CLIP-170's key to the dynein/dynactin pathway. Mol. Cell. Biol. *22*, 3089–3102.

STAR★METHODS

KEY RESOURCES TABLE

REAGENT or RESOURCE	SOURCE	IDENTIFIER
Antibodies		
Mouse anti-α-tubulin	Sigma-Aldrich	Cat#T6199; RRID:AB_477583
Rat anti-tyrosinated-α-tubulin	Thermo Fisher	Cat#MA1-80017; RRID:AB_2210201
Mouse anti-acetylated-tubulin	Sigma-Aldrich	Cat#T7451; RRID:AB_609894
Rabbit anti-CAMSAP2	Proteintech	Cat#17880-1-AP; RRID:AB_2068826
Rat anti-EB1 + EB3	Absea	15H11
Rabbit anti-CLIP170		2360
Chemicals, peptides, and recombinant proteins		
SiR-tubulin	Spirochrome	Cat#SC014
Janelia Fluor 646 HaloTag Ligand	Promega	Cat#GA1120
FuGENE 6	Promega	Cat#E2692
Lipofectamine 2000	Invitrogen	Cat#11668019
B27	Gibco	Cat#17504001
Pen/strep	Gibco	Cat#15140-122
L-Glutamine	Gibco	Cat#25030-081
Boric acid	Sigma	Cat#B6768
Borax (sodium tetraborate decahydrate)	Sigma	Cat#B9876
HEPES	Sigma	Cat#H3375
Poly-L-lysine	Sigma	Cat#P2636
Laminin	Roche	Cat#11243217001
Neurobasal medium	Gibco	Cat#21103049
10x (HBSS)	Gibco	Cat#14185045
Nitric acid	Emsure Merck	Cat#100456
Doxycycline-hyclate	Abcam	Cat#ab141091
PEI MAX	Polysciences	Cat#24765
Hygromycin B gold	InvivoGen	Cat#ant-hg-1
Puromycin	InvivoGen	Cat#ant-pr-1
Gibson Assembly Master Mix	Thermo Fisher	Cat#A46629
Experimental models: Cell lines		
HeLa Kyoto	Narumiya S., Kyoto University	CVCL_1922
COS-7	ATCC	CVCL_0224
U2OS	ATCC	CVCL_0042
RPE1	ATCC	CVCL_4388
HT1080	J. Klumperman, UMC Utrecht	CVCL_0317
HEK293T	ATCC	CVCL_1926
Experimental models: Organisms/strains		
Female Pregnant Wistar rats	Janvier Labs	N/A
Recombinant DNA		
EB3N (1-189)-VVDfast-mCl3-iLID	This paper	RRID:Addgene_190165
EB3N (1-189)-VVDfast-Halo-iLID	This paper	RRID:Addgene_190166
iLID-mCl3-DCX	This paper	N/A
iLID-mCl3-MAP7	This paper	N/A
iLID-mCl3-MAP7N(1-301)	This paper	RRID:Addgene_190167
iLID-mCl3-MAP7MTBD(59-170)	This paper	N/A
iLID-mCl3-MAP7D3	This paper	N/A

(*Continued on next page*)

Continued

REAGENT or RESOURCE	SOURCE	IDENTIFIER
iLID-mCl3-MAP7D3N(1-309)	This paper	N/A
iLID-mCl3-MAP7D3MTBD(55-174)	This paper	N/A
CLIP115N(1-309)-mCl3-iLID	This paper	N/A
iLID-mCl3-Tau0N4R	This paper	N/A
iLID-mCl3-miniTau0N4R(140-342)	This paper	N/A
iLID-mCl3-Tau0N4R MTBD(186-310)	This paper	N/A
iLID-mCl3-Tau0N3R	This paper	N/A
iLID-mCl3-MAP2C	This paper	N/A
iLID-mCl3-MAP2CMTBD(300-393)	This paper	N/A
SspBmicro-mCh-p60	This paper	RRID:Addgene_190168
LAMP1-Halo	This paper	N/A
Halo-Rab6A	This paper	RRID:Addgene_190171
Halo-KDEL	This paper	N/A
mCh-CLIP170	This paper	N/A
pSIN-TRE-EB3N-VVD-mCl3-iLID	This paper	RRID:Addgene_190169
pSIN-TRE-SspB-mCh-p60	This paper	RRID:Addgene_190170
psPAX2	D. Trono, EPFL	RRID:Addgene_12260
pMD2.G	D. Trono, EPFL	RRID:Addgene_12259
Software and algorithms		
FIJI	ImageJ	https://imagej.net/software/fiji/downloads
ComDet plugin	ImageJ	https://github.com/ekatrukha/ComDet
Faster Temporal Mean plugin	ImageJ	https://github.com/marcelocordeiro/MedianFilter-ImageJ
Membrane Displacement Analysis Macro	Spits et al.[60]	N/A
MtrackJ	Smal et al.[61]	N/A
Sigma Plot	Systat Software Inc.	7
Excel	Microsoft	Office16
Prism	Graphpad	9
MetaMorph	Molecular Devices	7.10.2.240

RESOURCE AVAILABILITY

Lead contact

Further information and requests for resources and reagents should be directed to and will be fulfilled by the lead contact, Anna Akhmanova (a.akhmanova@uu.nl)

Materials availability

Opto-katanin plasmids are available on Addgene.

Data and code availability

- All data reported in this paper will be shared by the lead contact upon request.
- This paper does not report original code.
- Any additional information required to reanalyze the data reported in this paper is available from the lead contact upon request.

EXPERIMENTAL MODEL AND SUBJECT DETAILS

Cultured cells

HeLa, U2OS, RPE1, COS-7, HT1080 and HEK293T cells were cultured in Dulbecco's Modified Eagle Medium (DMEM; Sigma) supplemented with 10% Fetal Bovine Serum (FBS; Corning), 100 U/ml penicillin and 100 μg/ml streptomycin (1% Pen Strep; Sigma). Cells were incubated at 37 °C with 5% CO_2. Cells were routinely tested for mycoplasma contamination using LT07-518 Mycoalert assay (Lonza).

Rats

Experiments were conducted in line with institutional guidelines of Utrecht University, and conducted in agreement with Dutch law (Wet op de Dierproeven, 1996) and European regulations (Directive 2010/63/EU). The animal protocol has been evaluated and approved by the national CCD authority (license AVD1080020173404). Female pregnant Wistar rats were obtained from Janvier, and embryos (both genders) at embryonic (E)18 stage of development were used for primary cultures of hippocampal neurons. The pregnant female rats were at least 10 weeks old and were not involved in any other experiments.

METHOD DETAILS

DNA constructs

All microtubule anchor constructs and the SspB-mCh-p60 construct were cloned into a pB80 backbone containing 6 x GGGGS linkers in between protein segments described previously[17] using Gibson Assembly. Mouse katanin p60 described previously[15] was used for the SspB-mCh-p60 construct. Human MAP7 and MAP7D3 coding regions described previously[27] were used as a template for iLID-mCl3-MAP7, iLID-mCl3-MAP7$_N$(1-301), iLID-mCl3-MAP7$_{MTBD}$(59-170), iLID-mCl3-MAP7D3, iLID-mCl3-MAP7D3$_N$(1-309) and iLID-mCl3-MAP7D3$_{MTBD}$(55-174). Human EB3 construct[62] was used as a template for EB3$_N$-VVD-mCl3-iLID and EB3$_N$-VVD-Halo-iLID constructs. Human 0N4R and 0N3R Tau construct[63] was used as a template for iLID-mCl3-Tau0N4R, iLID-mCl3-mini-Tau0N4R(140-342), iLID-mCl3-Tau0N4R MTBD(186-310) and iLID-mCl3-Tau0N3R. Rat MAP2C construct[64] was used as a template for iLID-mCl3-MAP2C and iLID-mCl3-MAP2C$_{MTBD}$(300-393). Mouse DCX construct[65] was used as a template for iLID-mCl3-DCX. Rat CLIP115 from[66] was used as a template for CLIP115$_N$(1-309)-mCl3-iLID. LAMP1-Halo was cloned by replacing mGFP with HaloTag in LAMP1-mGFP[67] using Gibson Assembly. Halo-Rab6A was cloned by replacing eGFP in eGFP-Rab6A[68] with HaloTag using Gibson Assembly. Halo-KDEL was cloned using Halo-Rab6A; A KDEL-encoding sequence (5'-AAAGACGAGCTATGA-3') was inserted replacing Rab6A using overlapping primers and restriction enzyme cloning, and an ER targeting sequence derived from Heat Shock Protein family A member 5 (HSPA5; 5'-ATGAAGCTCTCCCTGGTGGCCGCGATGCTGCTGCTGCTCAGCGCGGCGCGGGCC-3') was inserted directly in front of the HaloTag using Gibson Assembly. The mCh-CLIP170 construct was made by cloning rat brain CLIP170(192-4597) cDNA[69] into a StrepII-mCherry-C1 vector by restriction enzyme cloning. For making a stable cell line, EB3$_N$-VVD-mCL3-iLID and SspB-mCh-p60 were cloned into a pSIN-TRE lentiviral backbone as described in [70] containing either a hygromycin or puromycin resistance cassette respectively, also replacing rtTA with rtTA2^S-m2.[48] psPAX2 and pMD2.G lentiviral packaging constructs were a gift from D. Trono (EPFL, Lausanne, Switzerland).

Cell transfection

Transfection of HeLa, RPE1, COS-7 and U2OS was performed using FuGENE 6 (Promega) according to manufacturer's instructions using a ratio of 3 μl FuGENE 6 per 1 μg DNA.

Rat neuron isolation and culture

Coverslips were submerged in 65% nitric acid for two days followed by 4 washes with demi water of 1 hour each. Coverslips were then baked in an oven at 200 °C for 2 hours and cooled coverslips coated with a coating solution of 1.25 μg/mL laminin and 37.5 μg/mL PLL in 0.1 M Borate buffer (2.48 g/L Boric Acid, 3.8 g/L Borax, pH 8.5) overnight. Coverslips were washed 4 times with sterile MQ water for 1 hour per wash and incubated in neuron culture medium, Neurobasal medium (Gibco) supplemented with 2% B27 (Gibco), 0.5 mM L-glutamine (Gibco), 15.6 μM glutamate (Sigma), 100 U/ml penicillin and 100 μg/ml streptomycin (1% Pen Strep; Gibco), at 37 °C 3 days prior to plating neurons. Rat primary hippocampal neurons were isolated from the hippocampi of embryonic day 18 pups.[71] Hippocampi were gently washed in cold 1x Hank's Balanced Salt Solution (HBSS) 3 times, then incubated in 4 mL HBSS with 10 μL trypsin per hippocampi at 37 °C for 15 min, gently mixing every 5 min. Hippocampi were gently washed 3 times with 37 °C HBSS, leaving 4 mL HBSS after the last wash. Neurons were dissociated by pipetting hippocampi up and down until homogenous and plated at 100,000 cells per laminin and PLL coated coverslip in a 12 well plate. Cells were cultured in neuron culture medium and incubated at 37 °C with 5% CO_2.

Neuron transfection

Neurons were transfected on the 7th day *in vitro* (DIV7) with 1 μg EB3$_N$-VVD-mCl3-iLID, 2 μg SspB-mCh-p60 and 100 ng LAMP1-HaloTag using 3.3 μl Lipofectamine 2000 (Invitrogen), in Neurobasal medium with 0.5 mM glutamine.[72] After transfection neurons were gently washed in warm Neurobasal medium and returned to a mix of half conditioned and half fresh neuron culture medium.

HaloTag labeling

HaloTag dye JF646 (Promega) was diluted in DMSO to 200 μM, aliquoted and stored at -20 °C. Just prior to labelling a HaloTag aliquot was thawed and diluted 1:1000 in prewarmed cell media, vortexed for 5 s and incubated on cells for 15 min. Cells were washed 3 times with prewarmed cell culture PBS and then returned to cell media, live cell imaging was conducted over the next 5 hours.

Lentivirus production

HEK293T were plated at 30-35% in a 10 cm dish. The following day a transfection mix was prepared inside an Eppendorf containing: 15 μg pSIN-TRE-SspB-mCh-p60 or pSIN-TRE-EB3$_N$-VVD-mCl3-iLID, 10 μg psPAX2, 5 μg pMD2.G, optiMEM (for 1.2 mL final

volume) and 90 μL MaxPEI (1 mg/mL Polyethylenimine, Polysciences). The transfection mix was vortexed at low speed and incubated for 10 min before adding dropwise to the dish of HEK293T cells. Medium was refreshed the following day, discarding conditioned medium. The next day medium was refreshed, this time harvesting and storing the supernatant at 4 °C. The following day supernatant was also harvested and combined with the medium harvested the day before and cells were discarded. Medium was filtered through 0.045 μm filter to remove debris after which it was applied to an Amicon Ultra-15 filter column (Merck, UFC903029) and centrifuged for 30 min at 3000 rpm to purify virus. Remaining supernatant containing virus was aliquoted and stored at -80 °C until used for cell transduction.

Cell line transduction and selection

HT1080 cells were plated in a 12 well plate at 20-25% the day before. On the day of transduction, cell medium was refreshed with medium containing 6 μg/mL polybrene (Merck, TR-1003-G). Virus was thawed on ice and gently homogenized with a pipette before adding to cells at several different concentrations (1-20 μL virus per well). Medium was refreshed 24 hours later and 400 μg/mL hygromycin (Hygromycin B gold, InvivoGen, ant-hg-1) or 3 μg/mL puromycin (InvivoGen, ant-pr-1) was added 48 hours after transduction to select for pSIN-TRE-EB3$_N$-VVD-mCl3-iLID or pSIN-TRE-SspB-mCh-p60 containing cells respectively. Hygromycin or puromycin was also added to a well of cells not infected with lentivirus to ensure that untransduced cells are successfully eliminated before returning cells to normal cell culture medium. Single cells were plated in 96 well dishes, and resulting clonal cell lines were assessed for optimal expression levels upon 16-24 hrs treatment with 500 ng/mL doxycycline (Doxycycline-hyclate, Abcam, ab141091). Once clones containing both constructs were established, by first selecting good clones containing the pSIN-TRE-EB3$_N$-VVD-mCL3-iLID construct and then repeating all the steps to introduce the pSIN-TRE-SspB-mCh-p60 construct, low dark state activity and blue light induced microtubule severing was also assessed to identify the best performing clone. We refer to this clonal cell line as HT1080 pSIN EB3$_N$ p60.

Microscopy

Spinning Disc

Spinning disk confocal microscopy was performed on an inverted research microscope Nikon Eclipse Ti-E (Nikon), equipped with the perfect focus system (Nikon), Nikon Plan Apo VC 100x N.A. 1.40 oil objective (Nikon) and a spinning disk-based confocal scanner unit (CSU-X1-A1, Yokogawa). The system was also equipped with ASI motorized stage with the piezo plate MS-2000-XYZ (ASI), Photometrics PRIME BSI back illuminated sCMOS camera (version USB 3, Teledyne Photometrics) and controlled by the MetaMorph 7.10 software (Molecular Devices). Lasers were used as the light sources: 488 nm 150 mW (Vortran Stradus 488, Vortran Laser Technology), 561nm 100 mW (OBIS 561-100LS, Coherent) and 639 nm 150 mW (Vortran Stradus 639, Vortran Laser Technology). We used ET-GFP filter set (49002, Chroma) for imaging of proteins tagged with mClover3; ET-mCherry filter set (49008, Chroma) for imaging of proteins tagged with mCherry; ET-Cy5 filter set (49006, Chroma) for imaging of proteins tagged with HaloTag JF646. 16-bit images were projected onto the sCMOS camera chip at a magnification of 63 nm/pixel. To keep cells at 37°C we used stage top incubator (model INUBG2E-ZILCS, Tokai Hit). For localized illumination iLas system was used and controlled with iLas software (Gataca Systems).

TIRF

Azimuthal TIRFM was performed on an inverted research microscope Nikon Eclipse Ti-E (Nikon), equipped with the perfect focus system (Nikon), Nikon Apo TIRF 100x N.A. 1.49 oil objective (Nikon) and iLas3 system (Dual Laser illuminator for azimuthal spinning TIRF (or Oblique) illumination and Simultaneous Targeted Laser Action including PhotoAblation; Gataca Systems). The system was also equipped with ASI motorized stage MS-2000-XY (ASI), Photometrics CoolSNAP Myo CCD camera (Teledyne Photometrics) and controlled by the MetaMorph 7.8 software (Molecular Devices). Stradus 488 nm (150 mW, Vortran), OBIS 561 nm (100 mW, Coherent) and Stradus 642 (110 mW, Vortran) lasers were used as the light sources. We used ZT405/488/561/640rpc ZET405/488/561/635m filter set (TRF89901, Chroma) together with Lambda 10-3 (Sutter Instrument) filter wheel, equipped with the emission filters ET630/75m and ET700/75m (from ET-mCherry 49008 and ET-Cy5 49006 filter sets, Chroma). 16-bit images were projected onto the CCD chip at a magnification of 45.4 nm/pixel. To keep cells at 37°C we used stage top incubator (model INUBG2E-ZILCS, Tokai Hit). Localized illumination was controlled with iLas software (Gataca Systems).

Widefield microscopy

Widefield imaging was performed using a Nikon Eclipse 80i upright microscope fitted with a Photometrics CoolSNAP HQ2 CCD camera and a CoolLED illumination system. Microscope was fitted with a set of Chroma filters, the following filters were used to image samples: ET-BFP2 (49021) to image Alexa Fluor Plus 405 or DAPI, ET-GFP (49002) to image mClover3, ET-mCherry (49008) to image mCherry, ET-Cy5 (49006) to image Alexa Fluor 647. A Plan Apo VC 60x N.A. 1.40 oil objective was used to image samples and Nikon NIS Br software was used to control the microscope.

Airyscan confocal microscopy

For fixed confocal imaging a Carl Zeiss LSM880 Fast AiryScan microscope fitted with 405nm, Argon Multiline, 561nm and 633 nm lasers and AiryScan and PMT detectors was used. A Alpha Plan-APO 100x/1.46 Oil DIC VIS objective was used to image samples and ZEN 2.3 software was used to control the microscope.

Live cell opto-katanin microtubule severing

U2OS/COS-7/RPE1/HeLa cells were seeded at 15% confluency on 25 mm glass coverslips inside a 6 well plate one day prior to transfection. Cells were transfected with 1 μg EB3$_N$-VVD-mCl3-iLID or EB3N-VVD-Halo-iLID and 2 μg SspB-mCh-p60 and

co-transfected with 50 ng HaloTag-Rab6A or 100 ng HaloTag-KDEL or incubated with 100 nM SiR tubulin in cell media overnight, then used for the experiment the following day, taking care to protect cells from blue, violet and UV light after transfection. For Neuron experiments neurons were prepared and transfected as described above. For HT1080 pSIN $EB3_N$ p60 cell experiments, cells were seeded at 20% confluency 2 days prior to the experiment and treated with 500 ng/mL doxycycline (Doxycycline-hyclate, Abcam, ab141091) for 18 hours prior to imaging. Cells were labelled with HaloTag dye if applicable (labelling protocol described above), then imaged on a Spinning Disc microscope (or TIRF microscope in the case of ER imaging), a 561 nm laser was used to image SspB-mCh-p60 with one 500 ms exposure (0.41 mW, 500 $\mu W/cm^2$) every 4 s or 60 s, a 642 nm laser was used to image JF646 HaloTag dyes or SiR tubulin with one 500 ms exposure (0.25 mW, 300 $\mu W/cm^2$) every 2 or 4 s, for localized activation a FRAP unit was used to apply one localized 113 ms pulse of 488 nm light (3 μW, 700 $\mu W/cm^2$) every 4 s. In the case of mClover3 anchor imaging / field of view activation, a 488 nm laser was used with one 500 ms exposure (0.25 mW, 300 $\mu W/cm^2$) every 4 s.

Local opto-katanin severing followed by immunostaining

For local severing experiments followed by immunostaining cells were plated on gridded glass bottom dishes (Ibidi, μ-Dish 35 mm, low Grid-500, #80156), so that the same cell could be found back after staining. For rat neurons, dishes were coated as described above. Cell transfection and localized severing was also performed as described above. Fixative was applied to the dish while still mounted on the microscope, objective was lowered immediately prior to application of fixative. Fixation and staining of samples were performed as described below. Samples were imaged on an Airyscan confocal microscope.

Live cell imaging of microtubule dynamics

U2OS cells were plated at 15% confluency on 25 mm glass coverslips inside a 6 well plate 1 day prior to transfection. Since overexpression of a fluorescent EB3 would compete with the EB3N anchor and therefore likely influence the results, we opted to overexpress the plus TIP mCh-CLIP170 to label the growing microtubule ends. U2OS cells were thus transfected with either 500 ng mCh-CLIP170 alone (control); 500 ng mCh-CLIP170 and 1 μg $MAP7_N$ anchor ($MAP7_N$); 500 ng mCh-CLIP170 and 1 μg $EB3_N$-VVD-Halo-iLID ($EB3_N$); or 500 ng mCh-CLIP170, 1 μg $EB3_N$-VVD-Halo-iLID and 2 μg SspB-mCh-p60 ($EB3_N$ + SspB-mCh-p60). Cells were labelled with HaloTag dye if applicable (labelling protocol described above), then imaged on a Spinning Disc microscope. Plus end dynamics were captured by imaging mCh-CLIP170 for control and $MAP7_N$ treatments using a 561 nm laser (0.41 mW, 500 $\mu W/cm^2$) for 500 ms/stream acquisitions over 50 seconds; or imaging $EB3_N$-VVD-Halo-iLID using a 642 nm laser (0.25 mW, 300 $\mu W/cm^2$) for 500 ms/stream acquisitions over 50 seconds for $EB3_N$ and $EB3_N$ + SspB-mCh-p60 treatment groups on a spinning disc microscope.

Immunofluorescence

For CAMSAP2 staining cells were fixed with ice cold methanol on ice for 15 minutes.

For EB1 + EB3 staining cells were first fixed with ice cold methanol on ice for 15 minutes followed by 15 minutes with 4% paraformaldehyde in PBS. Cells were permeabilized with 0.2% Triton-X in PBS for 2.5 minutes.

For fixed cell analysis of microtubule anchors, HeLa cells plated on coverslips transfected the day prior were either fixed in a dark room using a red lamp (DARK), or first placed in an incubator under blue LED lights (800 $\mu W/cm^2$) for 16 minutes prior to fixation (LIT). Cells were first fixed with ice cold Methanol at -20°C for 7 minutes, followed by fixation with 4% paraformaldehyde in PBS for 15 minutes at room temperature. Cells were permeabilized with 0.2% Triton-X in PBS for 2.5 minutes.

For analysis of mitotic cells, HT1080 pSIN $EB3_N$ p60 cell line plated on coverslips was treated with or without 500 ng/mL doxycycline (Doxycycline-hyclate, Abcam, ab141091) for 18 hours before fixing in DARK or after LIT conditions described above. Cells were fixed in 4% paraformaldehyde with 4% sucrose in MRB80 buffer prewarmed to 37°C for 15 minutes at room temperature. Cells were washed 3 times with PBS and then permeabilized with 0.1% Triton-X in PBS for 10 minutes at room temperature.

Neurons were fixed with 4% paraformaldehyde with 4% sucrose in MRB80 buffer prewarmed to 37°C for 12 minutes at room temperature. Neurons were subsequently washed 3 times with PBS, then permeabilized with 0.1% Triton-X in PBS for 10 minutes at room temperature.

Samples were blocked for 1 hour in blocking buffer consisting of 2% Bovine Serum Albumin with 0.05% Tween-20 in PBS before application of primary antibodies. Primary antibodies were diluted in blocking buffer and incubated on samples for 1 hour, antibodies used were: Mouse anti-α-tubulin (Sigma, T6199; dil 1:200), Rabbit anti-CAMSAP2 (Proteintech, 17880-1-AP; dil 1:300), Rat anti-tyrosinated-α-tubulin (Thermo, MA1-80017; dil 1:200), Mouse anti-acetylated-tubulin (Sigma, T7451; dil 1:200), rat EB1 + EB3 (Absea, 15H11; dil 1:10), Rabbit anti-CLIP170 (#2360, [73]; dil 1:250), Samples were washed 3 times with PBS then incubated with highly cross-preadsorbed secondary antibodies diluted 1:250 in blocking buffer and incubated for 1 hour, secondaries used were goat anti-mouse conjugated with Alexa Fluor Plus 405 (Thermo Fisher, A48255) and goat anti-rat conjugated with Alexa Fluor 647 (Thermo Fisher, A21247). Samples were washed 3 times with PBS and mounted with Vectashield with or without DAPI (Vector Labs). HeLa cells transfected with different anchors and stained for α-tubulin, EB1+EB3 or CLIP-170 were imaged with a widefield Nikon upright microscope, as were coverslips for the mitotic analysis of the HT1080 opto-katanin stable cell line. COS-7 cells, neurons stained for different microtubule populations or α-tubulin and local opto-katanin cutting and fixing experiments were imaged on a Zeiss LSM880 Fast AiryScan confocal microscope.

QUANTIFICATION AND STATISTICAL ANALYSIS

Fluorescence intensity measurement and normalization

Quantification of local fluorescence intensity was performed in Fiji, data was normalized in Excel and data plots were prepared in Graphpad Prism. For live cell imaging experiments a neighboring transfected or SiR-tubulin labelled cell was used for normalization to account for photobleaching over time using the following equation:

Normalized ROI intensity = (ROI intensity – background) / (neighbor intensity – background)

For live cell fluorescence intensity over time plots, the normalized fluorescence intensities were subsequently divided by the average of the first 5 measurements to also account for variability in construct expression or SiR-tubulin staining.

For the local microtubule severing and fixation experiments with and without recovery, intensity inside the area of microtubule severing was quantified using live cell videos as a reference for where microtubule severing occurred. Intensities were then normalized to the whole cell intensity using the following equation:

Normalized ROI intensity = (ROI intensity – background) / (whole cell intensity – background)

For the fixed anchor testing experiment tubulin staining and mCherry/mClover3 intensity was normalized to untransfected neighboring cells. This was done using the following equation:

Normalized ROI intensity = (ROI intensity – background) / (neighbor intensity – background)

Microtubule dynamics analysis

Microtubule plus end tracing and kymograph plotting was performed using MtrackJ, a custom built plugin for Image J,[61] kindly shared with us by I. Smal (Erasmus Medical Centre, Rotterdam, The Netherlands). Kymographs were further analyzed using Sigma Plot 7, and data plots using the means for each cell were prepared in Graphpad Prism.

Dynamic lysosome analysis

Non-dynamic lysosomes were first filtered out using the Faster Temporal Mean plugin (https://github.com/marcelocordeiro/MedianFilter-ImageJ). Dynamic lysosomes were then counted inside the ROI where microtubules were severed and in a comparable region where microtubules were not severed, using the ComDet plugin (https://github.com/ekatrukha/ComDet). Dynamic lysosome counts were normalized to the average of the first 10 frames in Excel. Data plots were prepared in Graphpad Prism.

Membrane dynamics analysis

Golgi and ER membrane dynamics were quantified using the Membrane Displacement Analysis Fiji Macro developed and described previously,[60] kindly shared with us by L. M. Voortman (Leiden University Medical Centre, Leiden, The Netherlands). The output of this optical flow algorithm expresses membrane displacement in pixel intensity where a higher intensity corresponds to a higher displacement and an intensity of 0 corresponds to no displacement. Therefore, in order to express membrane dynamics within a ROI, the mean pixel intensity was quantified and normalized to the average of the first 10 time points in Excel. Data plots were prepared in Graphpad Prism.

ER nodule counting

Number of ER nodules inside the ROI and in a comparable region of the same size were manually counted once per 25 frames and normalized to the average of the first 3 counts in MetaMorph 7.10.2.240. Data plots were prepared in Graphpad Prism.

Mitotic stage analysis

Mitotic cells were identified based on chromosome condensation and manually characterized into stages using α-tubulin and DAPI staining. Counts were tallied in Excel, and fractions were calculated for each treatment per experiment. Data plots were prepared in Graphpad Prism.

Statistical analysis

A Mann-Whitney U test was used to test for statistical significance. A P value below 0.05 was regarded as statistically significant.